Development and validation of computational tools for the characterization and analysis of non-linear plasma photonic crystals

Whitney Thomas

A thesis
submitted in partial fulfillment of the
requirement for the degree of

Masters of Science

University of Washington

2018

Reading Committee:

Uri Shumlak, Chair

James Riley

Program Authorized to Offer Degree:
Aeronautics & Astronautics

University of Washington

Abstract

Development and validation of computational tools for the characterization and analysis of non-linear plasma photonic crystals

Whitney Thomas

Chair of the Supervisory Committee:
Professor Uri Shumlak
Aeronautics & Astronautics

Plasma photonic crystals have the potential to significantly expand the capabilities of current microwave filtering and switching technologies by providing high speed (μs) control of energy band-gap/pass characteristics in the GHz through low THz range. While photonic crystals consisting of dielectric, semiconductor, and metallic matrices have seen thousands of articles published over the last several decades, plasma-based photonic crystals remain a relatively unexplored field. Numerical modeling efforts so far have largely used the standard methods of analysis for photonic crystals (the Plane Wave Expansion Method, Finite Difference Time Domain, and ANSYS finite element electromagnetic code HFSS), none of which capture nonlinear plasma-radiation interactions. This thesis describes a set of tools implemented in the Computational Plasma Dynamics Lab's WARPXM finite element multi-physics code to simulate, characterize, and analyze non-linear fluid effects of plasma photonic crystals. The model is validated against theory, linear numerical models, and experimental results. Additionally, novel cases are explored.

TABLE OF CONTENTS

LIST OF FIGURES

ACKNOWLEDGMENTS

The author wishes to express sincere appreciation to Prof. Uri Shumlak, and the following members of Prof. Mark Cappelli's plasma lab at Stanford: Fabio Righetti and Ben Wang. This research is supported by a grant from the United States Air Force Office of Scientific Research.

DEDICATION

To my parents.

Chapter 1

INTRODUCTION

Plasma based photonic crystals are a promising, and potentially powerful, method for controlling microwaves. Photonic crystals are optic materials consisting of a periodic structure that takes advantage of Bragg reflections to selectively transmit or reflect certain wavelengths of light. Plasmonic metamaterials are man-made materials that use electron oscillations at a metal-dielectric interface (surface plasmons) to achieve certain optical properties. Plasmonic photonic crystals combine the effects of photonic crystals and plasmonics in a single device. *Plasma* photonic crystals extend traditional metal based plasmonic photonic crystals by adding high speed control of important transmission characteristics.

Why make plasmonic photonic crystals out of plasmas?

- **Plasmas can access an under served frequency band**. Plasmon resonances can occur in the **THz range**, a underutilized portion of the electromagnetic spectrum.
- **Fast control of photonic crystal properties.** Plasmas are created when needed, with lifetimes in the μs, for fast reconfiguration of lattice characteristics.
- **Fast control of plasmonic properties**. Plasma resonant frequencies can be controlled through application of external EM fields.
- **High energy applications**. Absorption can be controlled through collisionality. Plasmas are not subject to phase-change at high temperatures.
- **Self organization**. Plasmas can produce stable (in the time scales of interest) periodic structures. Potential devices could take advantage of naturally occurring periodicity from plasma instabilities.

There exists a suite of techniques for predicting the behavior of both photonic crystals and plasmonics, which can be extended for use with plasmas. Generally, these tools assume a linear response (low temperature plasma, small amplitude fields).

This research aims to use high-fidelity plasma models to explore non-linear plasma photonic crystal behavior in the limit where these low temperature, small field assumptions break down.

As part of a Multi University Research Initiative grant from the Air Force Offices of Scientific Research, the work described in this thesis is the assembly of a suite of numerical tools for the characterization of plasma photonic crystals using a hierarchy of increasingly more complex (and physically accurate) models. Using these tools, the limits of validity of each model can be quantified. Perhaps the most exciting outcome will be the exploration of how higher order effects could be used to further functionalize plasma photonic crystals.

In this thesis, we will discuss what progress has been made towards that objective. Validation of the fluid model will be demonstrated, and the numerical exploration of a number of plasmonic photonic crystal effects will be reviewed. Finally, next steps outlined.

Chapter 2

WHAT ARE PLASMA PHOTONIC CRYSTALS?

To understand the theory and the motivation behind the investigation of plasma photonic crystals, it is helpful to have a firm understanding of both photonic crystals and plasmonic metamaterials.

2.1 Photonic crystals

Photonic crystals are optic materials consisting of a periodic structure that takes advantage of Bragg reflections to selectively transmit or reflect certain wavelengths of light. Light is transmitted or reflected based on its wavelength. The wavelength is determined by the characteristic length of the periodic structure. For example, chameleon skin, a naturally occurring example of a photonic crystal, controls the wavelength of light reflected through active tuning of a lattice of guanine nanocrystals on their skin[33].

Photonic crystals can come in many different forms and configurations:

- **Dimension**. Photonic crystals can be one, two, or three dimensional.

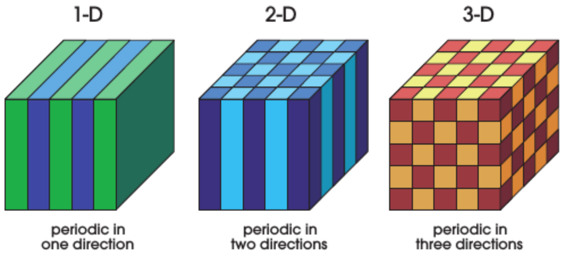

- **Periodicity**. They be either regular (can be described by their lattice structure), disordered[34], or regular with strategically located defects.

- **"Atom" shape.** The shape of the sub unit is unlimited. Spheres, oblate spheroids, holes, plates, squares, hexagons, ...
- **Material.** Photonic crystals can be composed of any material: dielectrics, metals, semiconductors, liquids, gasses, plasmas, and any combination thereof.

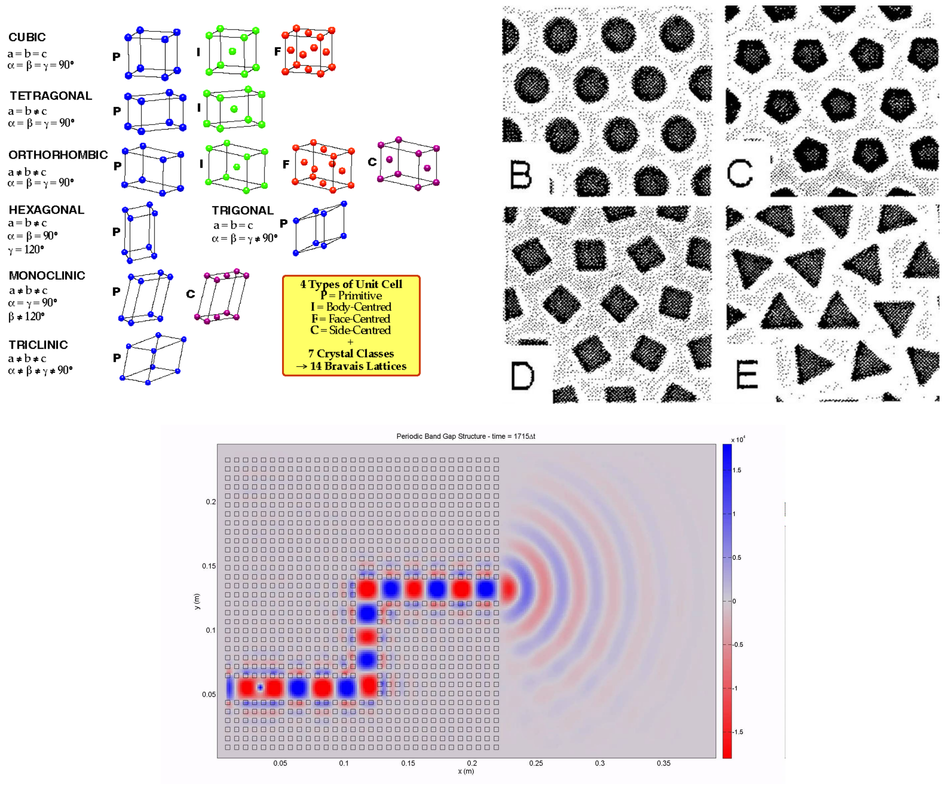

Figure 2.1: Photonic crystals are categorized by dimension, lattice type (top left), unit shape (top right), material, and whether or not they contain defects (bottom).

2.1.1 *History of photonic crystals*

Naturally occurring photonic crystals exist in both geology (opal) and biology (chameleon skin, butterfly wings, bird feathers, abalone and oyster shells). When in the optical range (periodic structures on the order of a few hundred nanometers) they appear iridescent to the human eye.

Figure 2.2: Opal and butterfly wings are naturally occurring examples of photonic crystals.

Human investigation of photonic crystals begins in 1887 when Lord Rayleigh showed that multi-layer dielectric stacks have a band gap. Called dielectric mirrors, they are currently used in thin-films for optical filters and paints.

Little progress was made for 100 years, until 1987 Eli Yablonovitch[42] and Sajeev John[9] published two seminal papers where they proposed that photons in a periodic dielectric structure behave similarly to electron waves in a crystal lattice. This allowed for the adaptation of band theory, which had seen considerable success in describing electron propagation in semiconductors, to optics. In 1991 Yablonovitch and Gmitter claimed to have created the first “photonic band gap” material, which they named Yablonovite, with a full band gap in the microwave frequencies[41].

A number of theorists, namely K. Ming Leung of Polytechnic University, and Kai Ming Ho of Iowa State University, became interested and modified their computational algorithms used for computing electron bands for use on photonic crystals. While they eventually proved that Yablonovite did not have a full band gap, they now had the tools to determine which lattice configurations would. In the subsequent years interest exploded. A wide variety of lattice structures were found to have either full or useful partial band gaps.

In 1998, Philip Russel at the University of Bath created the first photonic crystal fiber. Its utility was instantly recognized, as it could achieve information carrying capacities of over

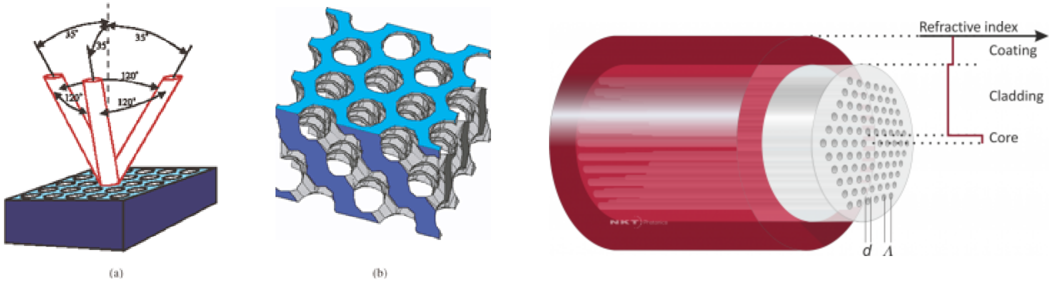

Figure 2.3: (Left) "Yablonovite", the first photonic crystal, developed by Yablonovitch and Gmitter in 1991. (Right) a photonic crystal optical fiber.

100 times that of a conventional fiber[10]. While there has been a lot of exciting research in photonic crystals and their applications in optoelectronics and optical computing, the photonic crystal fiber remains the only commercially successful two dimensional photonic crystal application to date.

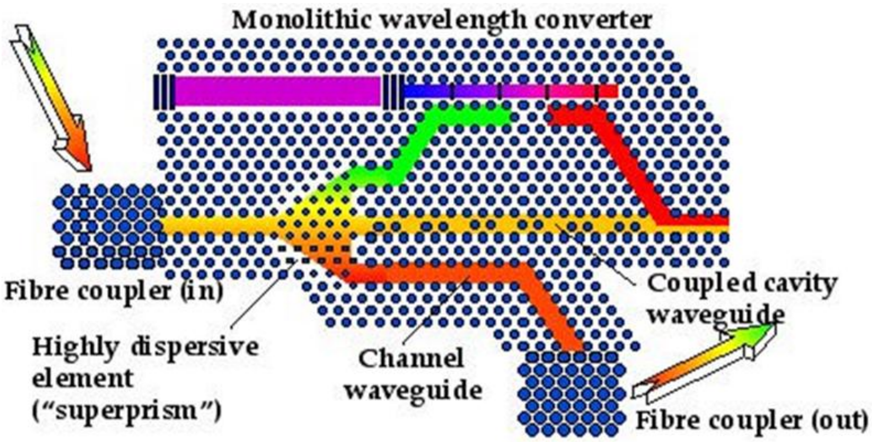

Figure 2.4: A concept for an optical circuit composed entirely of two-dimensional photonic crystal components[13]

Three dimensional photonic crystals films have only recently been able to make meaningful progress. Nanofabrication techniques are only now reaching the levels of accuracy and repeatability necessary to create large, tough films with decent optical properties. As a result, photonic crystal films have recently been used to increase the off-angle efficiency of photovoltaic panels[11].

2.1.2 Photonic crystal theory

Photonic crystals work through electromagnetic wave interference. In a random, inhomogeneous media, the waves reflect off of material interfaces at random points, with random directions. The direction of the original light would be hard to determine either from the reflection, or from the light that penetrates the material, as in frosted glass.

But if instead of being random, the materials were arranged in a regular, repeating pattern, the many reflections would add up. Patterns of constructive and destructive interference would emerge. The more reflections, the stronger and more defined the pattern. This is analogous to the Fourier transform of a single frequency wave train: the more periods of the wave that are captured, the sharper the peak in Fourier space. This pattern contains information not only about the original light, but also the material it's traveled through.

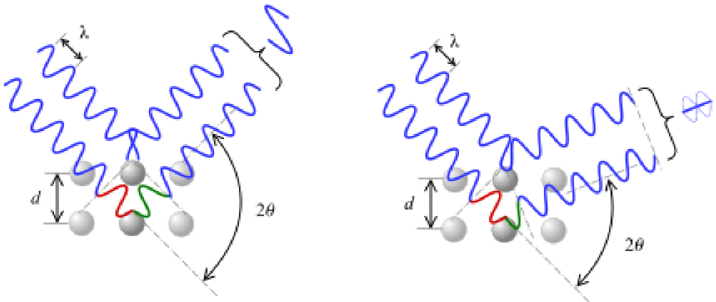

Figure 2.5: Graphical representation of Bragg's Law. Wikipedia: Bragg's Law.

In a material with consistent spacing, this results in an orderly diffraction pattern that is simple to predict. The angle of incidence for the strongest constructive interference of a cubic lattice can be easily calculated from Bragg's law,

$$2d \sin \theta = n\lambda, \tag{2.1}$$

where d is the lattice spacing, θ is the angle of incidence of the light, λ is its wavelength, and n is any positive integer.

Crystallography takes advantage of the information contained in diffraction patterns to reconstruct the crystalline structure of a material. If a third material is added, or the pattern is not a simple cubic lattice, the diffraction pattern becomes much more complex.

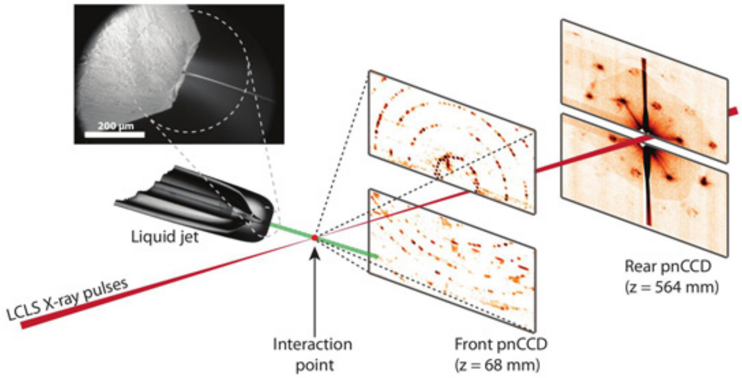

Figure 2.6: An example of crystallography being used to determine the structure of proteins[2].

A photonic crystal uses the same principles to solve the inverse problem: instead of using the diffraction pattern to find the crystal structure, the crystal structure is modified to achieve a desired diffraction pattern. More specifically, a crystal structure is created that achieves total reflection in most, or all directions, for a particular frequency. This is called a band gap.

Band theory

Band theory was developed to describe the electron energies allowed in a solid. For an insulator, these energies occur at discrete wavelengths corresponding to the atoms electron orbitals. For a conducting gas, all energies and momentums are possible. But for electrons in a conductor or semiconductor, these allowable states are discrete, but vary gradually with the momentum, forming continuous "bands." A *band gap* is a range of energies that do not contain any transmission bands.

This same concept can be modified for electromagnetic plane waves in a lattice of spatially varying permittivity. In this case, the eigenstates (allowable spatial configuration of the field) and eigenvalues (frequency) of solutions to the electromagnetic wave equation on a periodic media, where $\epsilon(x)$, can be found with Floquet-Bloch theory for periodic ODEs (as used with the Schrodinger Eq to find electron bands in a lattice),

$$\mathbf{H}_{\mathbf{k}n}(\mathbf{r}) = \mathbf{u}_{\mathbf{k}n}(\mathbf{r})e^{i\mathbf{k}\cdot\mathbf{r}} \tag{2.2}$$

$$\hat{\Theta}\mathbf{H}(\mathbf{r}) = \left(\frac{\omega}{c}\right)^2 \mathbf{H}(\mathbf{r}) \ : \ \hat{\Theta}\mathbf{H}(\mathbf{r}) \equiv \nabla \times \left(\frac{1}{\varepsilon(\mathbf{r})}\nabla \times \mathbf{H}(\mathbf{r})\right), \tag{2.3}$$

where H is the Bloch state and u is a periodic function that has the same periodicity as the lattice, $u_k(\mathbf{r}) = u_k(\mathbf{r}+\mathbf{R})$ where $\mathbf{R}$ is a reciprocal lattice vector. The Bloch states and their frequencies can be found numerically either as solutions to an eigenvalue problem, or in the time domain by applying Bloch periodic boundary conditions to the lattice unit cell.[29]

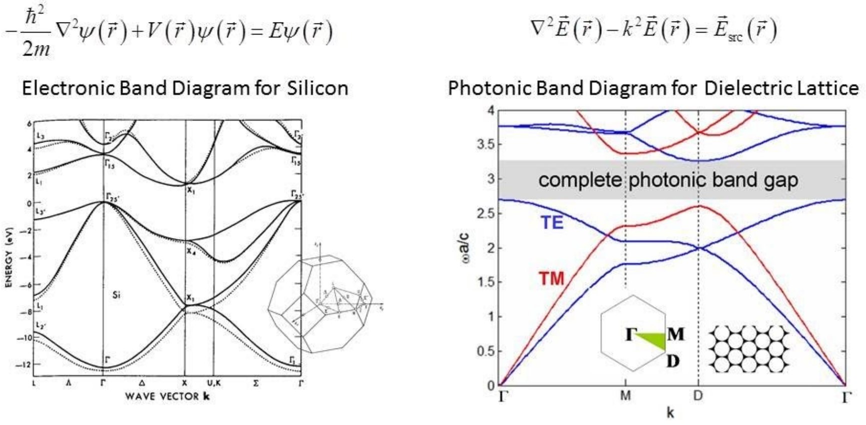

Figure 2.7: Electromagnetic waves in a photonic crystal are analogous to electrons in a semiconductor lattice. Examples of band diagrams for both cases[25].

Floquet-Bloch theory is no longer applicable when the finite nature of the photonic crystal becomes important, or if the crystal has defects. In these cases numerical simulation of Maxwell equations becomes necessary.

2.1.3 Numerical modeling

Flochet-Bloch theory is a powerful technique for describing the dispersion properties of a photonic crystal, and is generally sufficient when the crystal is large and uniform. But in some of the most interesting applications of photonic crystals, defects and non-uniformities are essential to the operation of the device: photonic crystal wave guides, steerable antennas, and optical transistors (see Figure 2.8. In these cases, numerical simulation becomes necessary.

Computational electrodynamics employs a number of different methods that are used for simulating photonic crystals:

- Finite difference frequency domain.
- Finite difference time domain: MIT Electromagnetic Equation Propagation (MEEP).
- Finite element: ANSYS High-frequency Structure Simulator (HFSS), COMSOL Multiphysics, WARPXM.
- Method of moments (MoM) or boundary element method (BEM): Keysight Momentum.

The work described in this report falls into this category.

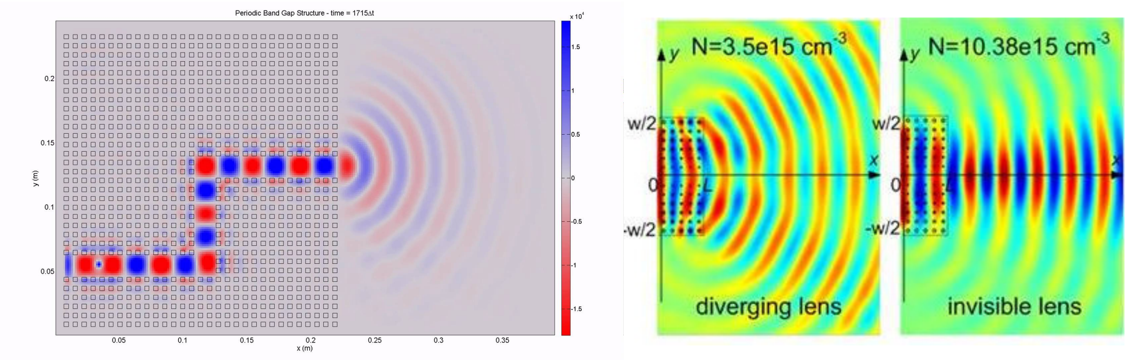

Figure 2.8: (Left) a photonic crystal band gap waveguide[17], (right) A tunable gradient plasmonic crystal.[35]

2.1.4 Methods of characterization

When considering photonic crystals as optical devices, the most important characteristics are transmittance, reflectance, and absorption. These can be easily measured experimentally, and are generally plotted versus frequency or wavelength of radiation. From *transmission spectra* band gaps can be identified and characterized. Import parameters of band gaps that can be interpreted from transmission spectra are: center, width, ratio (width/center), and attenuation.

Band gap maps are a convenient way to visualize how band gaps change due to lattice and material parameters.

Band diagrams plot band dispersion relations for wave vectors k that align with the major lines of symmetry (see Figure 2.7). A lot of information is contained in band diagrams, such as band gaps, transmission mode speeds, slow waves, band degeneracy, among other things.

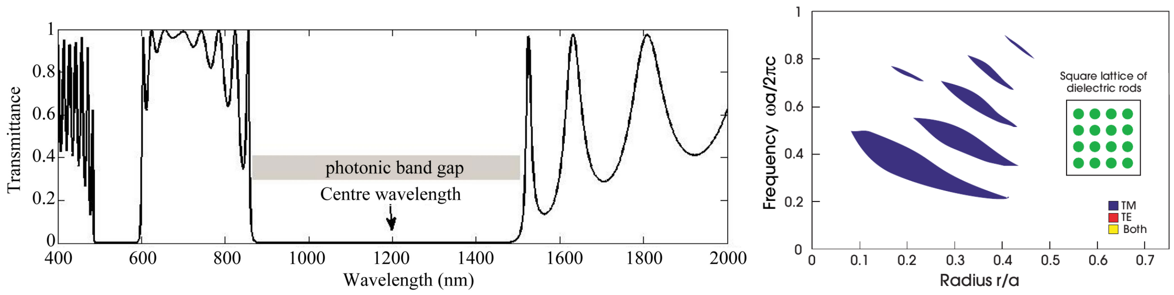

Figure 2.9: (Left) example of transmission spectra for TE radiation in a photonic crystal with photonic band gap highlighted. (Right) band gap map showing band gap evolution for a range of fill fractions r/a[8].

2.2 Plasmonic metamaterials

Plasmonic metamaterials take advantage of natural surface plasmon resonances on conductor-dielectric interfaces to absorb, couple, and re-radiate, energy at specific frequencies. They have proposed uses in cancer treatment [7], signal amplification[12], spectroscopy, and high efficiency photovoltaics[3].

Plasmonic metamaterials interact with light through surface plasmons. Field energy is absorbed into localized plasma oscillations that form at the surface of the metal/dielectric interface. On closed surfaces (cylinder in 2D, sphere in 3D) surface plasmons are stationary, and accumulate energy, producing fields many times larger than the driving wave.

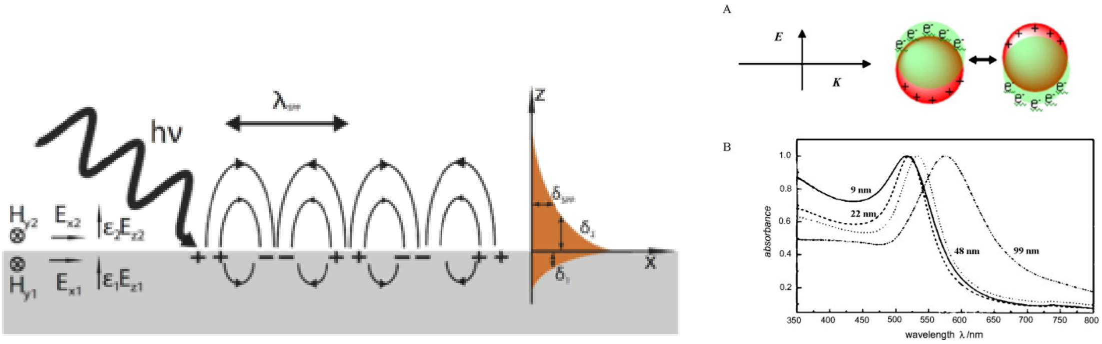

Figure 2.10: (Left) sketch of a surface plasmon, Wikipedia. (Right) surface plasmons on gold nanoparticles. [7]

For cylindrical rods the surface plasmon resonant frequency falls between $\omega_{pe}/\sqrt{3}$ and $\omega_{pe}/\sqrt{2}$, and is a function of fill fraction and mode number (see Figure 2.11. Each mode has a magnetic field arrangement as shown in the middle figure at right.

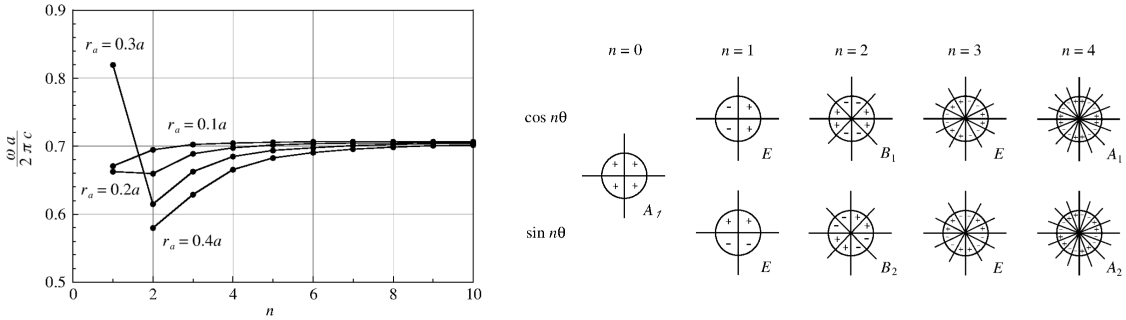

Figure 2.11: Mode frequencies and spacial configuration of modes for surface plasmon polaritons on a conducting rod[29].

2.3 *Plasmonic photonic crystals*

Plasmonic photonic crystals combine the properties of photonic crystals and plasmonic metamaterials. They can be constructed out of a combination of any conducting material (metals, semiconductors, plasmas) with a dielectric. They are characterized by an interesting interplay of photonic bands and plasmon resonances.

The same tools used in photonic crystals can be applied to plasma photonic crystals. For band characteristics of the infinite crystal, we can use Flochet-Bloch theory with a frequency dependent permittivity[27],

$$\hat{\Theta}\mathbf{H}(\mathbf{r}) = \left(\frac{\omega}{c}\right)^2 \mathbf{H}(\mathbf{r}) \ : \ \hat{\Theta}\mathbf{H}(\mathbf{r}) \equiv \nabla \times \left(\frac{1}{\varepsilon(\mathbf{r},\omega)\varepsilon_0}\nabla \times \mathbf{H}(\mathbf{r})\right) \tag{2.4}$$

$$\varepsilon_p(\mathbf{r},\omega) = 1 - \left(\frac{\omega_{pe}(\mathbf{r})}{\omega}\right)\frac{1}{1 - j(\nu_m/\omega)}, \tag{2.5}$$

where ω_{pe} is the electron plasma frequency, and ν_m is the collision frequency.

When $\omega < \omega_{pe}$, ε_p becomes negative. Surface plasmons can form and the crystal enters a plasmonic regime[29]. When confined to a closed surface (cylindrical in 2D and spherical in 3D) these plasmons are non-propagating, and present as “flat bands” in the band diagram (see figure at right), and result in band gaps.

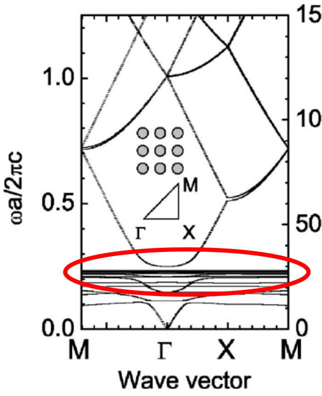

Figure 2.12: Band diagram for PC with $a = 2.5$ mm, $r = 0.5$ mm, and $n_e = 10^{13}\text{cm}^2$. Flat-bands due to surface plasmons are circled in red[27].

While traditional PC band gaps occur in frequency regions where forward propagating modes do not exist and reflection occurs, surface plasmon band gaps do have modes. But as they are stationary they do not transmit or reflect, but store energy (albeit temporarily).

When finite effects are important, numerical simulations of Maxwell equations are also applicable to plasma photonic crystals, with the added complication that permittivity is frequency dependent. This can be

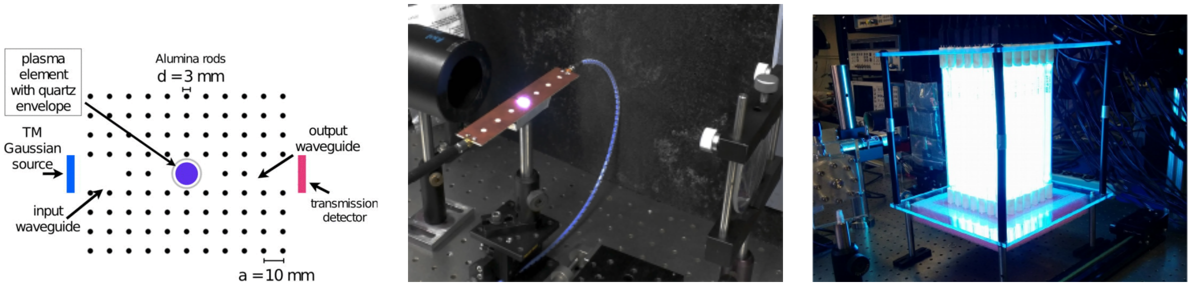

Figure 2.13: (Left) Plasma photonic crystal created by augmenting a traditional photonic crystals[36]. (Center) A microstrip photonic crystal device with a plasma element[39]. (Right) Plasma photonic crystals where plasma forms the principle material[37].

solved in several ways:

- Run a frequency domain simulation with a frequency dependent permittivity. Only gives a steady state solution, but is the fastest.
- Run a series of time domain simulations each with a single frequency and corresponding material permittivity. Shows dynamic response, but requires running many simulations.
- Self-consistently solve a physical model for the material behavior during the simulation that couples with the Maxwell's equations. This is the most accurate, can include physical effects that lead to non-linear behavior, but is computationally expensive.

2.4 Plasma photonic crystals

Finally, we come to plasma photonic crystals, or PPCs. PPCs are a sub-type of plasmonic photonic crystal distinguished by their use of plasmas for the conducting material. They can be formed either by augmenting traditional photonic crystals made of dialectics or metals, or as the primary conducting component.

2.4.1 History

Though plasma photonic crystals were being studied theoretically in the years before, Osamu Sakai at Kyoto University in 2005 is the first to publish experimental verification of a 2D plasma photonic crystal composed of an array of micro-discharges.[26]

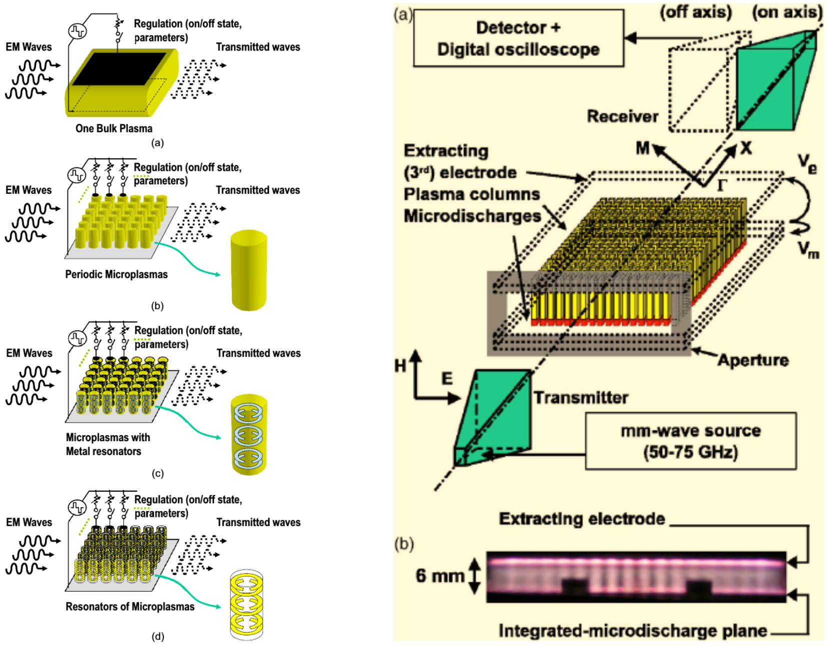

Figure 2.14: (Left) possible PPC devices as proposed by Sakai[28]. (Right) a microplasma array used by Sakai, et al as a plasma photonic crystal device[26].

Sakai argues in a review paper published in 2012 that plasmas can be integrated into periodic structures to create many new optical materials with exciting properties like tunable band-gaps, and a negative refractive index.[28]

In 2014 the AFOSR puts out a call for proposals for a multi-university grant "Control of Coherent Structures in Plasmas for Reconfigurable Metamaterial-Based Devices" and is awarded to a team headed by Mark A. Cappelli at Stanford, and includes L. Raja (University of Texas, Austin), J. Hopwood (Tufts University), C. Randall (Penn State), R. Wirz (UCLA), and Uri Shumlak (University of Washington).

2.4.2 Current state of field

To date, a number of plasma crystal experimental results have been published. In one dimension: plasmas functionalizing a microstrip [39], and a dielectric-plasma stack [].In two dimensions: all plasma micro-discharge arrays [26, 27, 40], tunable self-organized plasma discharges [5], plasma discharge tube arrays [37, 38], plasmas as functional unit in metal or dielectric PC [39, 14, 22].

Simulations have been conducted using a modified plane wave method[23], FDTD[6], and finite elements EM codes[37, 39, 24]. None have yet used fluid plasma models to self-consistently solve field and plasma interactions.

2.4.3 Challenges and areas of inquiry

All experimental and theoretical research performed up to this point centers around low energy applications. The wave energy deposited in the columns is assumed to have a negligible effect. As plasmas offer some of their greatest benefits over traditional materials at high powers, this is an important, and understudied, area of research.

High power EM waves could effect the plasma, and by it transmission characteristics, in several ways:

- *Plasma deformation.* If the field amplitude is sufficiently large, and wavelength long enough, the plasma will eventually develop regions of lower or higher electron density. As electron density drives plasmon frequency, and the dielectric constant, these changes could be detectable in the transmission spectra.
- *Plasma heating.* In a collisional plasma, currents driven by the incident radiation will resistively generate heat. This heating could cause changes in the device performance, if high enough.
- *Ionization-recombination.* When fields are strong enough that local concentrations due to the plasma exceed the ionization energy, ionization will occur. This is already a problem in high powered radar and communications antenna at high altitudes, and most research has been in mitigating this breakdown. Ionization in a plasma photonic crystal could be used to create passively functional devices.

The research reviewed in this thesis lays the groundwork for understanding all three of these effects, beginning with plasma deformation.

Chapter 3

NUMERICAL EXPERIMENT DEVELOPMENT FOR THE INVESTIGATION OF PLASMA PHOTONIC CRYSTALS

A two-dimensional, plasma-vacuum photonic crystal is simulated in the WARPXM computational framework using a coupled Maxwell-plasma fluid model. To establish the accuracy of the model, band diagrams and transmission spectra generated from the simulations are compared with Drude model simulations (both within WARPXM and in other software) and experiment. To develop a better understanding of the many types of plasma photonic crystal phenomenon, a numerical exploration of various plasmonic and photonic crystal effects is undertaken using WARPXM. Once we have confidence in the model, and our understanding, predictions are made on where non-linear plasma-radiation coupling effects might be seen, and are explored through further simulations.

3.1 Determination of scope

PPCs fall into two main categories, depending on how the plasma is integrated:

- **Plasma enhanced photonic crystal.** These are traditional photonic crystals made of a metal or dielectric that uses a plasma to alter the transmission characteristics. These plasmas can be active -a permanent plasma ignited and controlled by some secondary means- or passive -ignited in defects or field concentrations when field strengths reach a critical level.
- **Full plasma photonic crystal.** In this case, the entire crystal is composed of a periodic plasma. These PPCs should behave similarly to metallic photonic crystals, with the added benefit of active control of important lattice and material parameters over short time scales.

We have chosen the second type for several reasons. First, metallic and semiconductor 2D photonic crystals are fairly well researched, and plenty of tools exist for understanding and predicting their transmission characteristics. Secondly, there a quality experimental results available for direct comparison [37]. Finally, an all plasma photonic crystal exhibits interesting coupling behavior between plasmon and lattice resonances that could prove interesting.

For simplicity, the lattice parameters (lattice configuration, lattice constant, and fill fraction) are varied separately from the plasma parameters (density, temperature, and collisionality). In actual devices, where micro plasmas are created in free space by lasers or discharges, this may not always be the case, but by decoupling these parameters we can better understand the effects of each, and lay the foundation for more physically complete models in the future.

This research is funded by an exploratory grant on plasma photonic devices in the 100 GHz to 1 THz range. This implies plasma densities of $10^{20} - 10^{22}$ m-3, and lattice constants from 10 mm to 100 microns. While this regime includes devices beyond current engineering capabilities, both in size and density, this will likely not be the case for long.

3.2 Mathematical models that capture the relevant plasma dynamics

The physics important to the behavior being investigated must be taken into account when choosing an appropriate model. In the case of plasma photonic crystals, the important physics is the interaction of plasma with electromagnetic waves. This can happen in several ways:

- **EM wave-free electron interactions.** Important at frequencies at or below the electron plasma frequency, and plasma scales larger than the electron skin depth.
- **EM wave-bound electron interactions.** Bound electrons absorb and emit radiation in PHz to EHz range ($10^{15} - 10^{18}$ Hz).
- **EM wave-magnetized plasma interactions.** Here, strong interactions happen at the electron cyclotron frequencies.
- **EM wave-ion interactions.** As for free electrons, strong interactions happen near

the ion plasma frequency and on scales larger than the ion skin depth.

Bound electrons are obviously well outside our frequencies of interest, so can safely be neglected. Cyclotron frequency is a function of magnetic field strength. Static magnetic fields are not a necessary component of plasma photonic crystals, so can be neglected in most devices.

Ion plasma frequencies for typical laboratory plasmas are in the MHz to low GHz range: just outside our range of interest, but close enough that they should probably be taken into consideration at some point.

This leaves EM wave-free electron interactions as the most important. Individual electrons interact with EM fields through the Lorentz force,

$$\mathbf{F} = m_e \frac{d\mathbf{v}}{dt} = -e(\mathbf{E} + \mathbf{v} \times \mathbf{B}). \tag{3.1}$$

3.2.1 The Drude model

If we instead consider a homogeneous collection of many electrons with a constant density (in time), the above can be rewritten as an evolution equation for the momentum density, $\mathbf{p} = n_e m_e \mathbf{v}$, of a continuous electron fluid. If we also add a sink for momentum lost due to collisions with the heavier ions, we get the Drude model,

$$\frac{d\mathbf{p}}{dt} = -\frac{e}{m_e}\left(\rho\mathbf{E} + \mathbf{p} \times \mathbf{B}\right) - \nu\mathbf{p}, \tag{3.2}$$

where ρ is the electron mass density, ν is the electron-ion collision frequency, and the electric E and magnetic B fields are evolved through Maxwell's equations,

$$\nabla \cdot \mathbf{E} = \rho_c/\epsilon_0 \;:\; \nabla \cdot \mathbf{B} = 0 \tag{3.3}$$

$$\nabla \times \mathbf{E} = -\frac{\partial \mathbf{B}}{\partial t} \;:\; \nabla \times \mathbf{B} = \mu_0\epsilon_0\frac{\partial \mathbf{E}}{\partial t} + \mu_0\mathbf{J}. \tag{3.4}$$

Despite its simplicity, the Drude model is a powerful equation. It can capture EM wave reflection, dispersion, and absorption in metals and plasmas. When applied on a finite conductor, it can model surface plasmons. It also explains important macroscopic material properties of conductors like the electron plasma frequency, the dispersion relation for EM waves in a plasma, and the frequency dependent permittivity.

In fact, the Drude model, coupled with Maxwell's equations, can explain most common electrodynamic phenomenon: waveguides, antennas, radio wave reflection off the ionosphere, plasmonics, plasmonic photonic crystals, and more.

But electron motion can be driven by more than just EM fields. If we are to consider hotter plasmas, or stronger fields, effects like pressure gradients, time varying densities, and ionization-recombination need to be considred.

3.2.2 Fluid plasma-Maxwell models

The Drude model can be expanded to include these effects by self consistently evolving density and pressure, and adding the necessary pressure gradient and source terms. Since density, and velocity, can now no longer be assumed to be divergence free, the full convective derivative should be included. As should be expected, adding compressible fluid effects results in well known compressible fluid equations. Below we have Navier-Stokes equations with some additional terms,

$$\begin{aligned} \frac{\partial \rho_\alpha}{\partial t} + \nabla \cdot (\rho_\alpha \mathbf{v}_\alpha) &= \Gamma_{ion} - \Gamma_{rec} && (3.5) \\ \frac{\partial}{\partial t}(\rho_\alpha \mathbf{v}_\alpha) + \nabla \cdot (\rho_\alpha \mathbf{v}_\alpha \mathbf{v}_\alpha + \mathbb{P}_\alpha) &= q_\alpha n_\alpha (\mathbf{E} + \mathbf{v}_\alpha \times \mathbf{B}) + \sum_\beta \mathbf{R}_{\alpha\beta} + \sum_i m_\alpha (\mathbf{v}\Gamma)_i && (3.6) \\ \frac{\partial \varepsilon_\alpha}{\partial t} + \nabla \cdot (\epsilon \mathbf{v}_\alpha + \mathbf{v}_\alpha \cdot \mathbb{P}_\alpha + \mathbf{h}_\alpha) &= -\mathbf{v})\alpha \cdot (q_\alpha n_\alpha \mathbf{E} + \sum_\beta \mathbf{R}_{\alpha\beta}) + \text{ion-rec source terms,} && (3.7) \end{aligned}$$

where the subscript α denotes the fluid species (ion, electron, neutral, etc.)

The results shown in this thesis will neglect ionization-recombination $\Gamma_{ion}, \Gamma_{rec}$, inter and intra-species collisions $\mathbf{R}_{\alpha\beta}$, and all ion or neutral dynamics $\alpha \neq n, i$. The effects of these terms will be examined in future work.

The Boltzmann plasma model and its moments

While we have arrived at a fluid plasma model from the simple Drude model by adding physical effects, we could have come at this from another direction. Starting from the microscopic description of a plasma as a collection of individual particles all moving in different directions at different speeds, we can create a hierarchy of models of progressively *decreasing* fidelity. First by invoking statistical mechanics to approximate the sea of individual particles each with its own equation of motion, as a smooth probability function $f(\mathbf{x}, \mathbf{v}, t)$ with a single equation. The result is the Boltzmann plasma model,

$$\frac{\partial f_\alpha}{\partial t} + \mathbf{v}_\alpha \cdot \frac{\partial f_\alpha}{\partial \mathbf{x}} + \frac{q_\alpha}{m_\alpha} \left(\mathbf{E} + \mathbf{v} \times \mathbf{B} \right) \cdot \frac{\partial f_\alpha}{\partial \mathbf{v}} = \left. \frac{\partial f_\alpha}{\partial t} \right|_c . \tag{3.8}$$

While the degrees of freedom in the Boltzmann equation are dramatically reduced from a full particle description, there is still a lot of information stored in velocity space that isn't always necessary. In many cases, the distribution function can be well described through a hierarchy of integrated values, or moments. For example, a normal distribution can be exactly described by its first three moments, corresponding to the macroscopic values of density, momentum, and temperature.

Equations for the evolution of moment variables are arrived at by taking moments of the Boltzmann equation[30]. The first five moments (density, three velocity directions, and isotropic pressure) give what is known as the 5N-moment plasma fluid model, and is closely related to the Navier-Stokes fluid model. Additional moments describe departures from normal distribution functions: anisotropies in pressure can be captured in the 10-moment model, heat flux in the 13-moment model[18], etc.

3.3 Washington Approximate Riemann Solver (WARPXM) code

The models mentioned above have all been implemented numerically by others in the WARPXM computational framework[19]. WARPXM is an unstructured Discontinuous Galerkin finite element code developed in the Computational Plasma Dynamics Laboratory at the University of Washington. The framework was developed primarily for solving multi-scale, coupled, non-linear equation sets commonly found in plasma physics. The code is highly modular, allowing for a virtually infinite combination of spatial discretizations, temporal discretizations, equation sets, and boundary conditions. Parallelization is achieved through spatial decomposition with MPI.

In this study the following preexisting capabilities were used:

- Maxwell field equations, Maxwell field equations with perfectly hyperbolic divergence cleaning [20], 5N-moment plasma fluid model [30], Maxwell-fluid model coupling.
- Third-order finite elements, Rusanov numerical flux between discontinuous element boundaries.
- Free slip and conducting wall boundary conditions.

The following modules were implemented for this work:

- Bloch periodic boundary conditions (see Appendix A)
- Open boundary conditions (see Appendix B)

3.4 Numerical models

Several photonic crystal numerical models were constructed.

3.4.1 Infinite two-dimensional crystal

The infinite crystal is useful as it can provide information about propagation bands and band gaps. For this model, a two-dimensional mesh of a single crystal unit cell is used. Bloch periodic boundary conditions (see Appendix A) are imposed on all boundaries. A plasma, or other material model, is initialized and evolved in the center subdomain. A complex field is evolved everywhere through two sets of Maxwell field equations (real and imaginary). The plasma and field are coupled through source terms.

A radial sinc function is initialized in the real field in order to excite a broad range of wave numbers in all directions. A series of simulations are run, each having a different $\mathbf{k}$

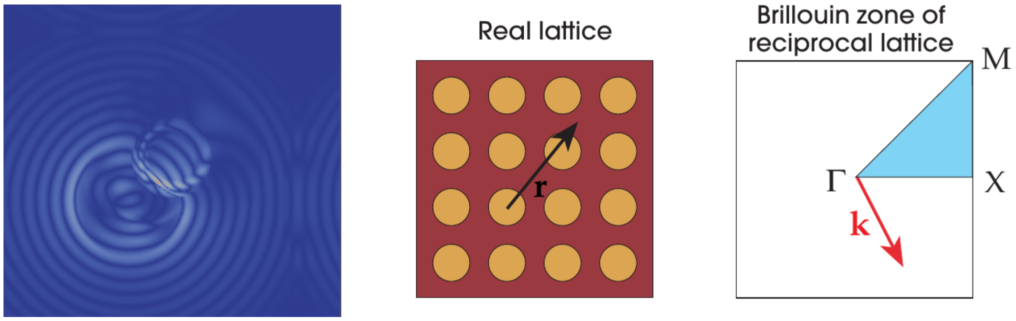

Figure 3.1: (Left) example unit cell crystal domain shortly after initialization. Contours are real electric field magnitude. (Right) the Brillouin Zone (smallest unit of symmetry) for a rectangular crystal lattice, with lines of symmetry and symmetry points used for determining important **k** wave vectors[8].

vector applied on the Bloch boundary conditions that corresponds to reciprocal points on crystal lines of symmetry. The region defined by this region on the reciprocal lattice is the Brillouin Zone.

The simulation is run long enough to allow for the emergence of constructively interfering modes. A Fourier analysis is performed on data collected at specific points in space to determine the frequency of these modes. Modes are then plotted per **k** to construct a band diagram.

3.4.2 Semi-infinite crystal

The semi-infinite crystal model is useful for studying the effect that lattice and plasma parameters have on transmission spectra. A number of columns ($n = 1 - 7$) are aligned in x in the center of the domain. Periodic boundaries in y simulate an infinite lattice perpendicular to EM wave propagation. A broad band pulse (sinc function) is propagated in x from left to right through the domain, and field values are probed at various locations in the region left of the columns.

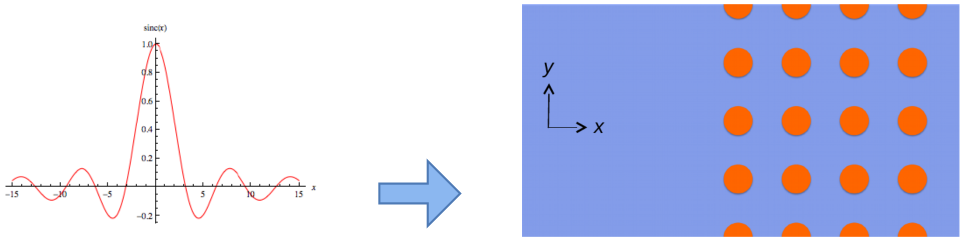

Figure 3.2: Simulation domain for semi-infinite crystal.

3.4.3 Finite crystal

Experimental devices compared in this study are finite (7x7) crystals. To capture the effect of diffraction around the finite edges of a crystal, a model was created for a 3x3, 5x5, and 7x7 two dimensional PPC.

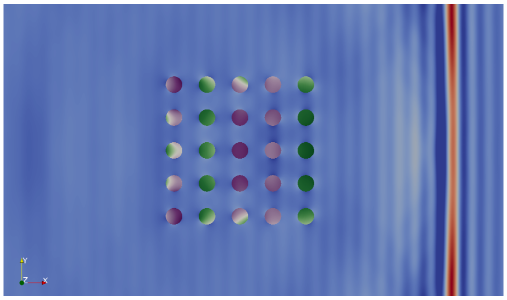

Figure 3.3: Example results from a 5x5 finite crystal simulation. Background contours (blue-red) are electric field magnitude. Column contours (purple-green) are electron momentum in y.

3.4.4 Single column

High resolution, single column models were used to study plasma dynamics under strong fields.

Chapter 4

VALIDATION OF THE NUMERICAL MODEL

As these simulations constitute the first attempt to model plasma photonic crystals at this level of physical detail, confirmation that the model reproduces expected results in the linear limit is necessary.

First, transmission spectra for a rectangular lattice photonic crystal are compared for the multi-fluid model and the Drude model, in the cold plasma (0.028 eV), weak field ($E_{max} = 1$ V/m), limit. Both simulations are done in WARPXM, with identical mesh and physical parameters.

Second, transmission spectra and band diagrams generated by WARPXM are compared with those generated by other E & M codes commonly used in photonic crystal analyses.

Finally, transmission spectra generated from WARPXM simulations are compared with experimentally generated spectra.

4.1 Fluid model vs the Drude model for a cold plasma

In the limit where plasma deformations are small ($\partial\rho/\partial t = 0$) and the plasma is cold ($p = \nabla p \approx 0$), as shown in the previous chapter, the equations for a 5-moment, ion-electron plasma can be reduced to the Drude model. Therefore, at low temperatures and energies, a plasma should behave much like an ideal conductor. To test this, both models were used to simulate a plasma photonic crystal, and transmission spectra were generated and compared over a wide range of plasma frequencies.

The fluid model at cold temperatures (0.028 eV) and weak electromagnetic fields ($E_{max} = 1$ V/m) was coupled with Maxwell equations. The Drude model was implemented by initializing the same plasma parameters as mentioned above, but only evolving the plasma through the Lorentz force term that couples with Maxwell's equations.

As expected, the results were identical. There was no discernible difference in the transmission spectra despite small changes in density in the full fluid model case.

4.2 *WARPXM vs ANSYS HFSS and Meep*

PPC simulations in WARPXM are compared with two well known software packages.

4.2.1 Transmission spectra

The ANSYS finite element electromagnetic code HFSS is an industry standard for the modeling of antennas and waveguides. HFSS's ability to handle complex 3D geometries and a variety of material properties has also proven useful in the simulation of photonic crystals[37, 38]. The software is limited in the types of materials it can model, plasmas not being among them.

The cold, weak field fluid model case simulated in WARPXM is compared with a similar Drude model simulation in HFSS.

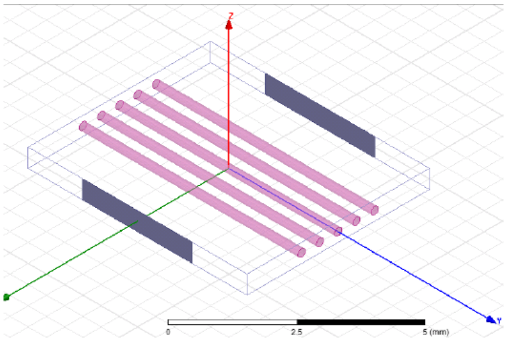

Figure 4.1: HFSS simulation domain, courtesy of F. Righetti.

The WARPXM simulation consisted of a 4 row semi-infinite two-dimensional case, with planar broad-band EM waves. The HFSS simulation was performed by F. Righetti at Stanford, and differed from the WARPXM case in that the broadcasting and receiving antennae had a finite size, and the domain was three-dimensional.

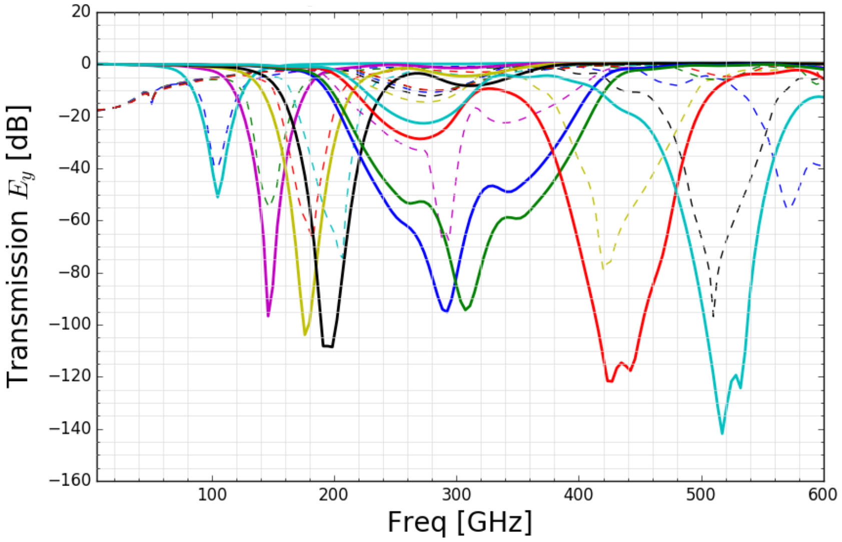

Figure 4.2: Transmission spectra for a range of plasma frequencies for similar cases in WARPXM (solid), and HFSS (dashed).

Both software show similar general behavior, though deviate in depth and width of band gaps. This difference could easily be accounted for by differences in simulation geometry. The narrow antenna in the HFSS simulation will create different interference points at different distances behind the array, making the transmission spectra sensitive to probe location.

4.2.2 Band diagram

Meep (MIT Electromagnetic Equation Propagation)[21] is an open-source finite-difference time-domain (FDTD)[32] electromagnetic code. Meep supports a wide variety of material models, including Drude. Bloch periodic boundary conditions give Meep the ability to simulate periodic materials, as well as allow for the study of lattice modes and the generation of band diagrams.

Bloch periodic boundary conditions were implemented in WARPXM (See Appendix). Band diagrams were generated with the fluid model and compared with results from Meep (see Figure 4.3). Results are reassuringly similar, and improve in correlation with increased resolution.

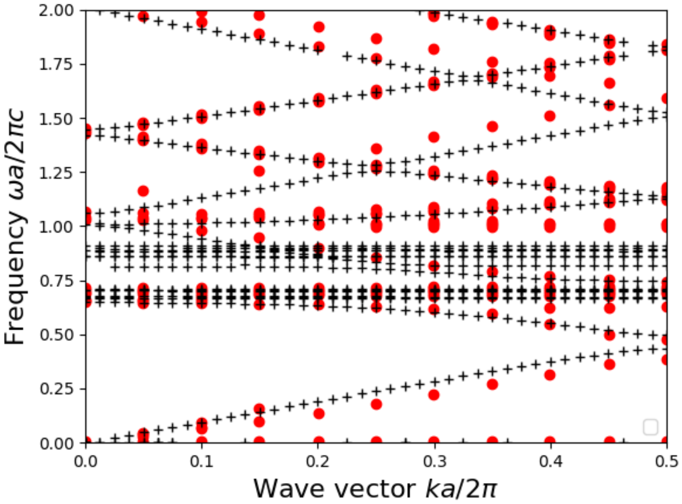

Figure 4.3: Photonic bands for a rectangular PPC with $f_{pe}c/a = 1$ and $r/a = 0.12$, calculated with WARPXM (red dots) and Meep (black +).

4.3 *Comparison with experiment*

M. Cappelli and B. Wang at Stanford constructed a plasma photonic crystal of a 7x7 array of plasma discharge tubes[37, 38] (see Figure 4.4). The discharge tubes contain an argon gas seeded with mercury. Quartz tubes have a lattice spacing of $a = 38.1mm$, and an inner radius of $r = 6.5$ mm. Variable amperage is the primary control of plasma parameters. Three amperages are chosen, with an estimated plasma density of $n_e = 1.1,\ 5.8,$ and 7.8×10^{17} m^{-3} ($f_{pe} = 3.0,\ ,6.9,$ and 8.0 GHz). Collision frequency is assumed to be $\nu = 1.0$ GHz. The measured spectra published in [37] are compared with HFSS simulations of a semi-infinite 7 row crystal, with a 1 mm quartz envelope ($\epsilon = 3.8$) and uniform density plasma with $r = 4.6$ mm.

In WARPXM, a finite 7x7 row crystal was also simulated with the same densities, temperatures, and plasma density profile, but without the quartz envelope or collisions. The results are compared with the experimental and HFSS spectra in Figure 4.5.

The WARPXM results (all in solid blue) mimic all the major features seen in the ex-

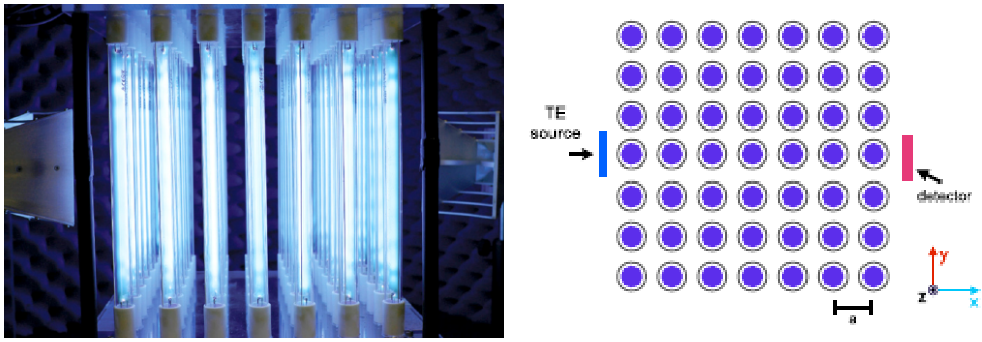

Figure 4.4: Stanford plasma photonic crystal experimental setup[37]. Quartz discharge tubes contain an argon gas seeded with mercury. Lattice spacing $a = 38.1$ mm, $r = 7.5$ mm.

perimental results. The experimental spectra tend to be broader, and shallower, which is consistent with simulations that have been run for non-uniform density profiles. The HFSS spectra (dashed lines) show a narrow band gap at 9 GHz that do not appear in either the experimental or WARPXM spectra, and is likely due to the quartz envelope. A small Fano resonance type feature occurs in the 7 and 8 GHz HFSS spectra around 6 GHz which is present in the experimental spectra, but not the WARPXM spectra. This could be a coupling between the plasma and quartz tube resonances. A WARPXM simulation with the quartz tube and non-uniform profile would be necessary to determine if this is the case.

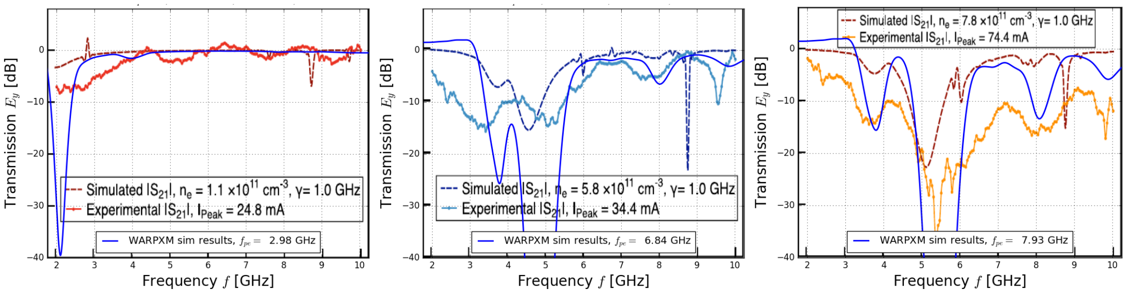

Figure 4.5: WARPXM results compared with Stanford plasma photonic crystal experimental and HFSS simulation results.

Chapter 5

NUMERICAL INVESTIGATION OF A PLASMA PHOTONIC CRYSTAL

The numerical model validated in the previous section provides a powerful tool for exploring many aspects of plasma photonic crystals. Below, a few of the more notable results are summarized.

5.1 Surface plasmon, photonic band gap resonance

Plasma density (and thereby the plasma frequency) has the strongest effect on transmission spectra. Even for small crystals where destructive interference from Bragg reflections is weak, significant energy is absorbed in plasmon oscillations. In Figure 5.1 up to 140 dB band gaps are present at the surface plasmon frequency ($\omega_{pe}/\sqrt{2}$). In comparison, the band gap associated purely with the photonic band gap (seen around the lattice frequency $f_a = c_0/a = 300$ GHz for $f_{pe} = 155 - 300$ GHz, and $600 - 750$ GHz) is never greater than 30 dB.

As the plasmon resonance frequency approaches the lattice frequency the character of the band gap changes dramatically. At $f_{pe} = 430 - 450$ GHz the band gap becomes broad and shallow as the surface plasmon resonance begins to couple with scattered frequencies. Since these band gap frequencies are not discrete, and can in some cases cover a range of continuous frequencies, it is possible that this an example of Fano resonance. Fano resonances have been observed in many photonic crystals and plasmonic metamaterials[15, 4]. Further work is needed to determine if this is really the case.

Beyond the Fano resonance, higher mode number resonances create a complicated transmission spectra which is much harder to decipher. In Figure 5.2 the transmission spectra of PPCs with plasma frequencies > 500 GHz have multiple deep band gaps that no longer

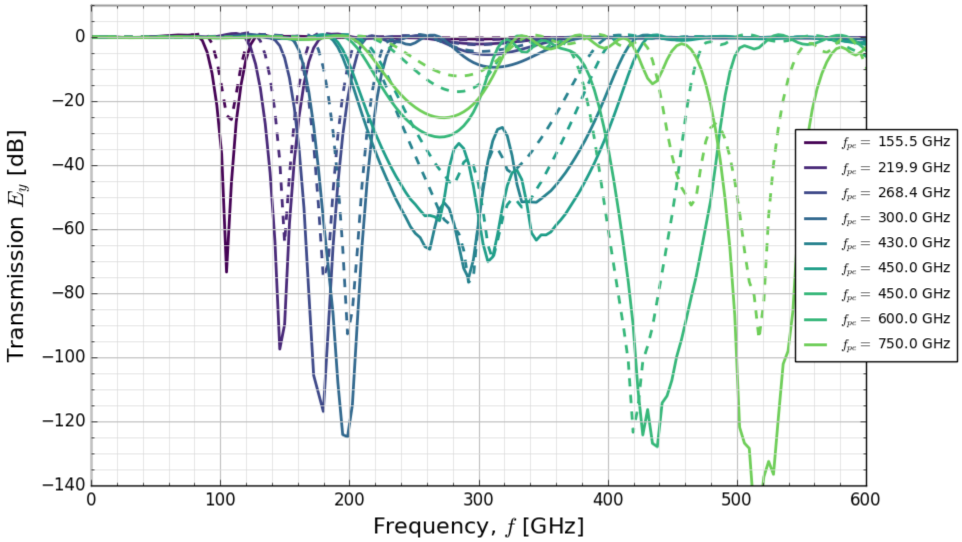

Figure 5.1: Transmission spectra for a range of plasma frequencies. Semi-infinite crystal with 4 rows, $a = 500$ microns, $r = 100$ microns (solid), $r = 75$ microns (dashed).

correspond to the plasmon frequency. They also include smaller band gaps at or above the plasma frequency where the dielectric constant is positive, between 0 and 1.

5.2 *Plasma temperature*

Plasma temperature has nearly insignificant effect on transmission characteristics in the collisionless, low resolution simulations. In Figure 5.3 the same 3 row PPC is simulated over a range of frequencies with two different temperatures, 0.028 eV (solid) and 100 eV (dashed). A temperature difference of nearly four orders of magnitude!

This is understandable. Temperature has no direct contribution to the plasma frequency or the effective permittivity, the two material parameters that determine the plasmonic and scattering responses. Temperature could indirectly effect the imaginary component of permittivity through the collision frequency ν_m, as it is a function of the mean free path

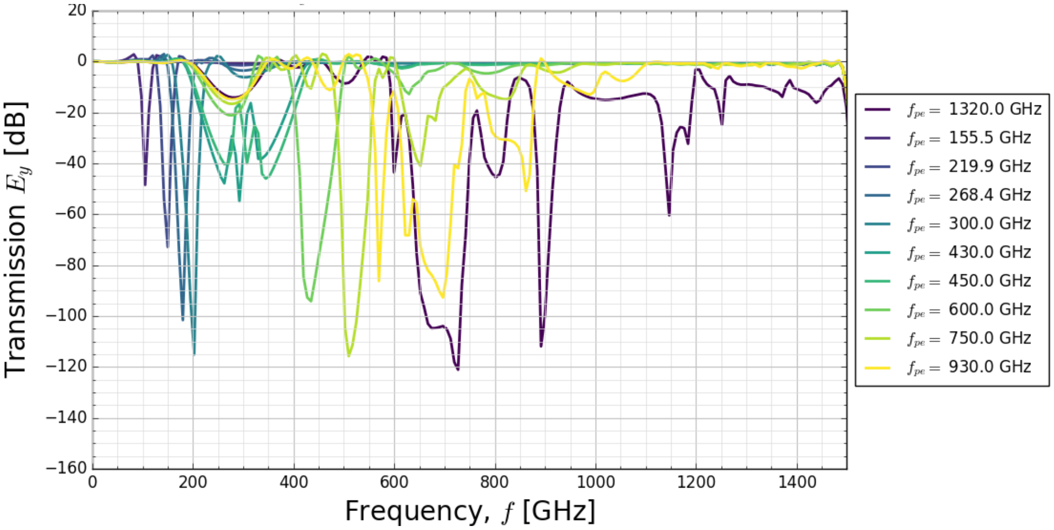

Figure 5.2: Transmission spectra for the same PPC case as Figure 5.1, now including $f_{pe} =$ 930 and 1320 GHz, showing the complex transmission spectra at frequencies much higher than the lattice frequency (300 GHz in this case).

$$\epsilon_r = 1 - \frac{\omega_{pe}^2}{\omega^2(1 + j\nu_m/\omega)} \tag{5.1}$$

As collisions are not included in these simulations, then this could not contribute here.

The temperature could indirectly contribute to the plasmon resonance frequency through the plasma frequency, which is a function of electron density. Electron density can only depart significantly from the ion density in regions on the order of the Debye length, which is a function of temperature

$$\lambda_D = \sqrt{\frac{\epsilon_o n e^2}{kT}} \tag{5.2}$$

Even at the 100 eV, the largest Debye length is less than the element size 5×10^{-6} m. Any density perturbations would not be resolved. Even if the Debye length were resolved (which we will explore in the next chapter) the EM wave energy would have to be large enough to drive a sizable density perturbation.

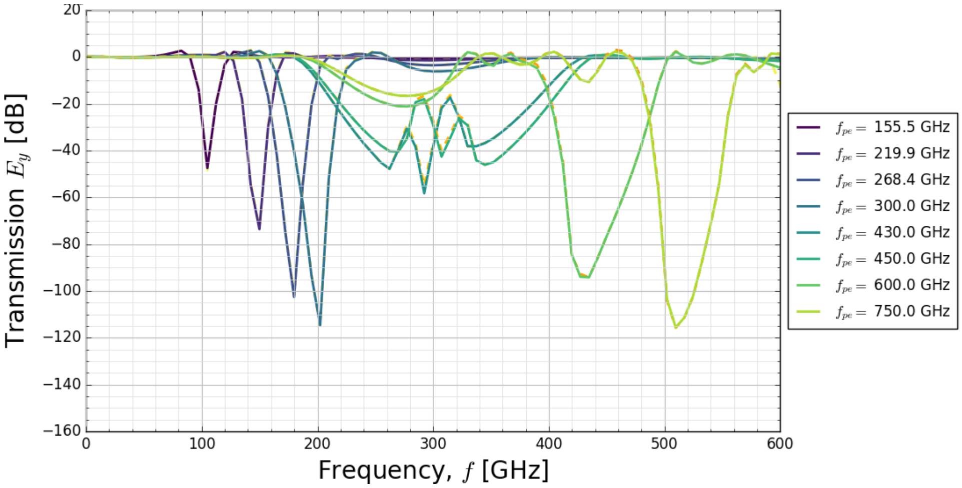

Figure 5.3: Transmission spectra at two different temperatures: 0.028 eV (solid) and 100 eV (dashed).

5.3 *Lattice parameters and transmission characteristics*

5.3.1 Fill fraction

The fill fraction, r/a, increases as the plasma columns take up a larger percentage of the space. As can be seen in Figure 5.1 this has several effects on the transmission spectra. The smaller columns (dashed lines) have narrower band gaps, and the Fano resonance is much less pronounced. Below the Fano resonance ($f_{pe} < 430$ GHz) the band gaps appear to be shifted to higher frequencies, and above the Fano resonance the opposite is true.

The upward shift in lower frequencies can likely be explained by the fact that higher mode number surface plasmons have a frequency that is a function of radius (see Figure 5.4). The shallowing is likely due to the increased free space between plasma columns allowing for more wave energy to make it through the crystal without meeting with a column.

The downward shift at higher frequencies is likely due to the fact that these hybrid band gaps are influenced by the mean space between column surfaces (not just center-to-center column spacing a) which will be longer as the column radius shrinks.

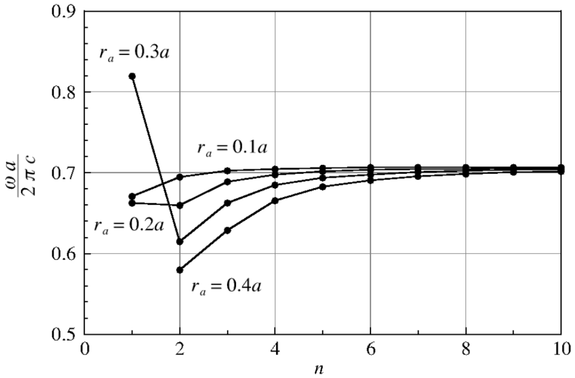

Figure 5.4: Surface plasmon polariton frequencies by mode number and fill fraction[29]. The smaller the fill fraction, the narrower the range of frequencies.

5.3.2 *Finite crystal*

Finite crystals behave similarly to the semi-infinite crystals (see Figure 5.5) except that the limited extent of the crystal allows for diffraction of large wavelengths. In these results the constructive interference of wavelengths on the order of the total crystal size ($\lambda = 1 - 3$ mm, or $f = 100 - 300$ GHz) have a greater than unity transmission coefficient!

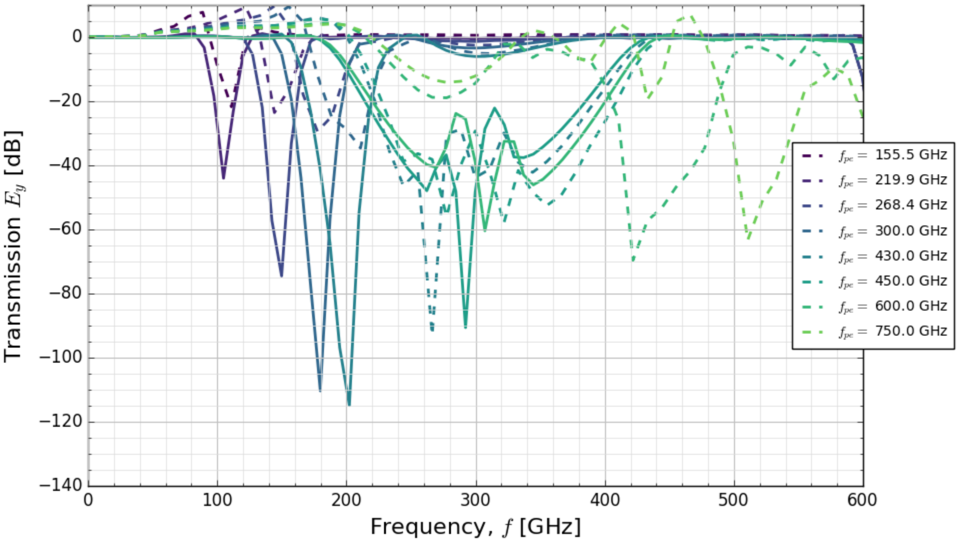

Figure 5.5: Transmission spectra for a semi-infinite 3 row (solid) vs finite 3x3 crystal (dashed).

Chapter 6

INVESTIGATION OF HIGH POWER MICROWAVE PPC INTERACTIONS

The numerical exploration of plasma photonic crystals described in the previous section has provided some groundwork on the investigation of non-linear plasma effects in plasma photonic crystals.

To review, high power EM waves could effect the plasma (and indirectly transmission characteristics) in several ways:

- *Plasma deformation.* If the field energy is strong enough, and wave length long enough, the plasma will eventually develop regions of lower or higher electron density. As electron density drives plasmon frequency, and the dielectric constant, these changes could be detectable in the transmission spectra.
- *Plasma heating.* In a collisional plasma, currents driven by the incident radiation will restively generate heat. This heating could cause changes in the device performance.
- *Ionization-recombination.* When fields are strong enough that local concentrations due to the plasma exceed the ionization energy, ionization will occur. This is already a problem in high powered radar and communications antenna at high altitudes, and most research has been in mitigating this breakdown. Ionization in a plasma photonic crystal could be used to create passively functional devices.

For this investigation, strong fields are considered to be $> 10^5$ V/m.

6.1 Plasma deformation

While it is a given that an externally applied electric field will generate a separation of charge on length scales on the order of the Debye length, this local change in electron density will only effect plasma-EM wave interactions if the deformation is large compared to the electron skin depth. Mathematically, this looks like,

$$\lambda_D \approx \delta_{pe} \quad \rightarrow \quad \frac{v_{th}}{\omega_{pe}} \approx \frac{c_0}{\omega_{pe}} \quad \rightarrow \quad v_{th} \approx c_o. \tag{6.1}$$

In most laboratory plasmas, and especially in those likely to be used in PPC devices, v_{th} will be many orders of magnitude smaller than the speed of light. This condition indicates that PPC devices will be highly resistant to changes in transmission characteristics in high fields.

The above line of reasoning is based on a static field picture, and does not include effects due to increased heating, or ionization that will likely become important once fields are strong enough. We will investigate the validity of these assumptions in the following sections.

6.1.1 Electron deformation due to strong EM fields

To capture the evolution of electron density profiles in a finite plasma under strong electric fields, a single column simulation was created. The left boundary gradually ramps the electric field from 0 to 10^7 V/m. Top and bottom boundaries are conducting wall, and the right boundary is open.

The most interesting feature observed is that unless the ramp rate is extremely slow, the electrons respond by oscillating at the surface plasmon frequency. The amplitude of this oscillation continues to increase as long as the field is applied. Eventually, the electric fields within the plasma column become many times that of the background field. This growth continues until the simulation fails.

The sloshing density profile is observed to reach over $3\times$ the background density at its peak, and as little as 10% on the low density side. The density profile is asymmetric: the high density sheath being about 5 Debye lengths thick, and the low density sheath extending to almost twice that. This is expected, as the lower density will have a larger Debye length.

Extrapolating out to longer times and larger oscillations, it could be expected that density

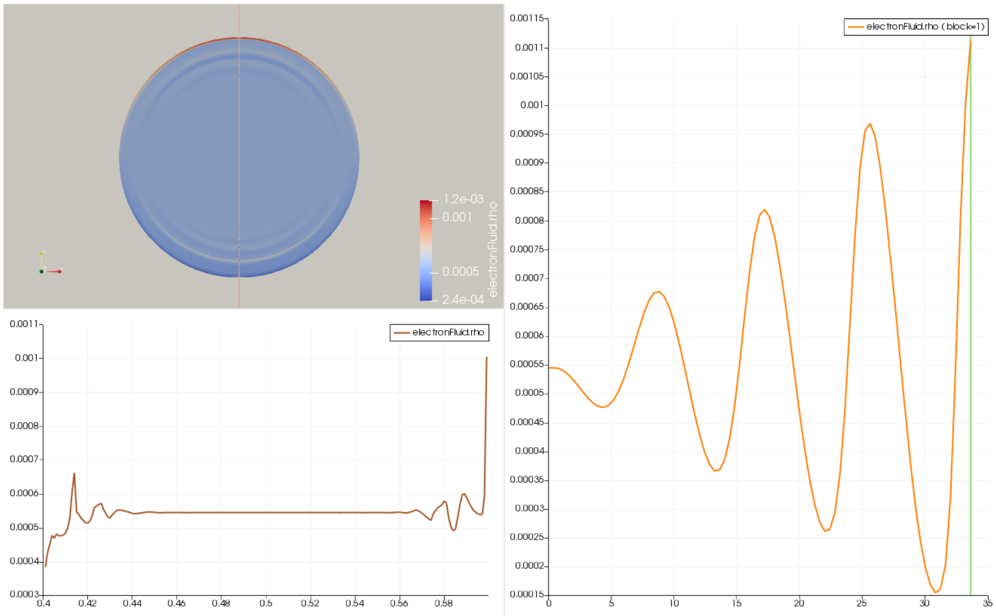

Figure 6.1: Electron density deformation under a strong, static electric field ($E = 10^7$ V/m). (top left) contours of electron density, (bottom left) cross-section of density, and (right) electric field strength inside plasma column over time.

perturbations will become large enough to deplete density in the core of the plasma. In that case, shifting band gaps will be expected.

It is not yet clear that this will happen. The large density perturbations of the $n = 0$ surface plasmon mode do appear to be gradually cascading energy to higher number modes. Further simulations at higher resolution over more plasma periods will be necessary to determine which effect wins out.

6.1.2 Effect of non-uniform density profiles on transmission characteristics

Non-uniform density profiles are important to resolve for several reasons. Most current methods generate diffuse plasmas, or have edge gradients due to wall interactions. Additionally, if plasma deformation due to strong fields becomes large enough, this will also cause non-uniform profiles. To understand how non-uniform profiles effect transmission spectra, as series of simulations was performed with a variety of density profiles (see Figure 6.2).

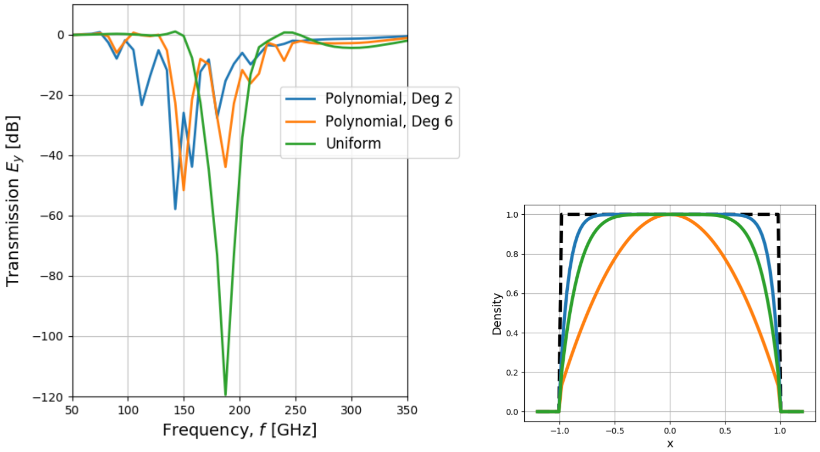

Figure 6.2: Transmission spectra of non-uniform density profiles for $f_{pe} = 100$ GHz.

In the figure above, results are shown for a low resolution simulation of the profiles shown at left. Higher resolution simulations, are underway, and data is currently being processed. These low resolution results show the spreading of band gaps to lower frequencies and shallowing of the peak band gap. The jagged, multi peaked character of the non-uniform density band gaps is an artifact of poorly resolving the density profile. In simulations where the Debye length is resolved, the band gap becomes much smoother.

These results confirm that non-uniformities much larger than the skin depth will have a significant effect on the transmission spectra. Current simulations on narrower non-uniformities show that effect disappearing. The conclusion is that density perturbations will have to be very large, and on the scale of the skin-depth to effect transmission spectra.

6.1.3 Ion dynamics

If electron deformation is large, and persists over long time periods, energy will inevitably leak into ion motion. No work has yet been done by anyone in the field on high power PPC devices and ion dynamics. Further work is planned to include ion dynamics once we feel that the question of high field electron dynamics has been sufficiently resolved.

6.2 Heating

Plasma heating has two parts, both of which could effect transmission spectra: increase in plasma temperature, and a non-negligible electron-ion collision frequency.

6.2.1 Temperature

In the previous chapter, we saw that temperature changes of 4 orders of magnitude had a nearly insignificant effect on transmission characteristics. Unless the higher temperature leads to new physical effects (Debye length becomes large enough to create a significant plasma sheath) then increased temperature will not significantly effect device performance.

This is highly desirable in devices designed for consistent operation though a range of energies.

6.2.2 Collision frequency

Electron collision frequency has a direct effect on the imaginary component of the plasmas effective dielectric constant (Eq. 2.5), which indicates absorption. Per [24] increased collision frequency broadens band gaps and increases wave energy absorption into the plasma.

WARPXM has the capability to include electron-electron, electron-ion, and electron-neutral collisions. Including these effects is planned for future simulations.

6.3 Ionization

In atmospheric air, the critical ionization field is around 10^6 V/m, which is within range of field levels in high powered microwave devices. Increased ionization can effect both the plasma density and plasma column radius. In the previous chapter, we show that band gap center frequency is strongly dependent on plasma density. We also showed that column radius has a significant effect on band gap width.

Neutral effects, including ionization-recombination, have recently been implemented in WARPXM. Simulations are planned for including ionization effects in PPC models.

Chapter 7

CONCLUSIONS

Plasma photonic crystals promise to be a powerful way to control high powered microwaves. Research into their construction, and control is still in its infancy. No serious investigation has yet looked into how high amplitude fields will effect plasma behavior, and transmission characteristics.

In this thesis we have reviewed the implementation and exploration of a PPC plasma-Maxwell model in the WARPXM framework. WARPXM is an unstructured, discontinuous Galerkin finite element code that is well suited for efficiently solving nonlinear hyperbolic problems on complicated geometries. Mesh decomposition allows for both effective parallelization, and physics decomposition. Additional capability was added for this work in the form of Bloch periodic and open boundary conditions. Bloch periodic boundary conditions allow for the analysis of properties of the ideal, infinite photonic crystal by finding crystal bands. Open boundary conditions facilitate the simulation of finite crystals in free space or open waveguides.

The plasma-Maxwell model was validated against a Drude-Maxwell model, both within WARPXM and by a well-known EM codes ANSYS HFSS and Meep. Model generated transmission spectra also showed good agreement with experimental results. It was proposed that the behavior could by modified through three effects: 1) fluid deformation, 2) energy absorption, and 3) ionization-recombination.

Plasma fluid deformation was first examined theoretically, and it was determined that any electron density deformation due to an incident field would likely not be large enough to significantly impact wave energy interaction as long as the temperature was low ($v_{Th} << c_0$). A high resolution simulation of a single column of 1 eV plasma acted on by a constant $1x10^5$

V/m field confirmed that electron deformation is contained within 5 Debye lengths of plasma edge.

The effect of non-uniform density profiles were also investigated, to determine the sheath thickness necessary to see a significant effect on transmission characteristics. Results confirm that deformed region must be on the scale of the electron skin depth.

The effect of energy absorption was investigated through simulating a wide range of temperatures. It was found that even when the temperature was changed many orders of magnitude, there was little effect on transmission spectra. This was supported theoretically by the fact that temperature has no direct effect on plasma frequency, the primary material characteristic that determines PPC behavior.

From these results we can so far conclude that PPCs are highly resistant to performance changes due to large amplitude fields, when considering only plasma deformation and heating. Work is continuing to determine to what field strengths and frequencies this remains the case. Collisions will be added to investigate energy absorption and plasma heating. Eventually, ionization will also be considered, as it promises to have a significant effect at high powers. A detailed description of next steps is outlined in the next section.

Chapter 8

FUTURE WORK

A number of questions remain that will be explored further in future work. In order of priority these are:

- **Examine reflection and absorption spectra.** When the plasma frequency approaches or exceeds the lattice frequency, the transmission structure becomes much more complicated. Band gaps due to Bragg reflections or plasmon resonances should show up as either reflected or absorbed energy. A better understanding of what effect causes which features will create a clearer understanding of how to control PPCs.
- **Confirm character of Fano type resonance.** A strong, Fano-type resonance occurs when $f_{pe} = \sqrt{2}f_a$. It is characterized by a rapid transition from transmission to bandgap over a few GHz. Understanding the important factors that control the resonance, and its quality, will help in the design of future devices. This could include lattice configuration, fill fraction, plasma density profile or absorption.
- **Continue search for field amplitude and frequency where fluid effects become important.** As field energies increase, more and more electrons will have to be displaced to neutralize the field. Where the density decreases, the Debye length will increase. At some point, the depleted region will grow to a size that is comparable to the column size, and the column shape will be deformed. As seen from the non-uniform density simulations, a sizable deformation in density will effect the transmission spectra.
- **Explore effects of collisions on transmission spectra and wave energy absorption.** Collisions are already known to have an effect on PPC transmission characteristics. They will also lead to increased energy absorption. Examining energy

absorption rates, and the effects on things like Fano resonance will be helpful.

- **Include ion dynamics in high field limit.** As field strengths become large, and electron deformation is sizable, the ions will eventually start to respond. Including ion dynamics will create a more complete picture.
- **Incorporate ionization-recombination, and other neutral effects.** Ionization energies of atmospheric air are with range of modern high power microwave sources. Studying the effects of ionization and recombination will be crucial to understanding PPC performance in these cases.

Appendices

Appendix 1

BLOCH PERIODIC BOUNDARY CONDITION IMPLEMENTATION IN WARPXM

Photonic crystals have a large amount of symmetry that can be beneficially exploited in developing numerical models, the most obvious being periodic boundary conditions. Unfortunately, many of the field modes in a periodic media will have spatial periods different from that of the material structure. Normal periodic boundaries enforce a single periodicity, resulting in the destructive interference of all waves that are not integer multiples of the domain length.

To get around this limitation, a phase shift ψ can be applied to a wave as it passes a boundary,

$$\mathbf{F}^1(\mathbf{x}) = \mathbf{F}^2(\mathbf{x})e^{j\psi}, \tag{A.1}$$

$$\mathbf{F}^2(\mathbf{x}) = \mathbf{F}^1(\mathbf{x})e^{-j\psi}, \tag{A.2}$$

where

$$\psi = \mathbf{k} \cdot \mathbf{a}, \tag{A.3}$$

and $\mathbf{F}$ is the field variable, superscript 1 and 2 denote the left and right boundaries, $k = 1/\lambda$ is the wave vector, and a is vector of periodic lengths in each direction.

This adds several complications: 1) the problem size is doubled due to the use of complex fields(real fields do not contain phase information), and 2) only one phase shift, and therefore only one spatial periodicity k, can be run per simulation.

As these boundary conditions are in effect replicating the same symmetry as Bloch theorem, they are commonly referred to as Bloch periodic boundary conditions. Similarly, the numerical model can also be used to find the eigenvalues and eigenstates of the photonic crystal. For further reading, please see the article by Celuch-Marcysiak, et al [1].

A.1 Implementation in WARPXM

In WARPXM, subdomains and virtual boundary conditions (BCs between subdomains) were harnessed to effect the Bloch periodic phase shift at unit cell boundaries.

A.1.1 Mesh

First, a mesh is created with subdomains that only meet other subdomains (not themselves) at periodic boundaries (seed Figure A.1). When the mesh is imported, all domain boundaries are tagged as periodic boundaries.

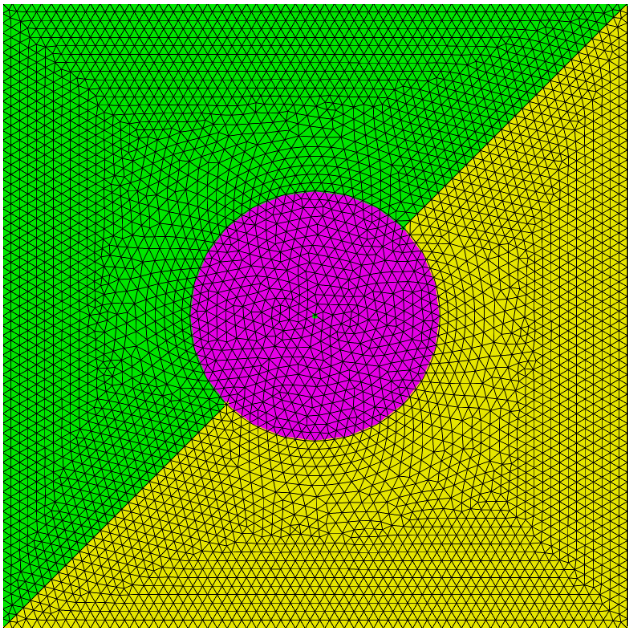

Figure A.1: Example of a mesh subdomain division necessary for two sets of Bloch periodic boundary conditions on a 2D domain.

A.1.2 Variables

Separate sets of real and imaginary variables are assigned to *each* subdomain, including the fluid variables. The real and imaginary variables will be evolved separately, only coupled at the Bloch boundary conditions.

Separate field variables in the upper and lower domain are necessary to allow for discontinuous solutions at periodic boundaries where the phase shift occurs. Considering this requirement, one of the vacuum domain variables can be assigned to the plasma domain, so as to reduce the required number of sets of variables (see Figure A.2).

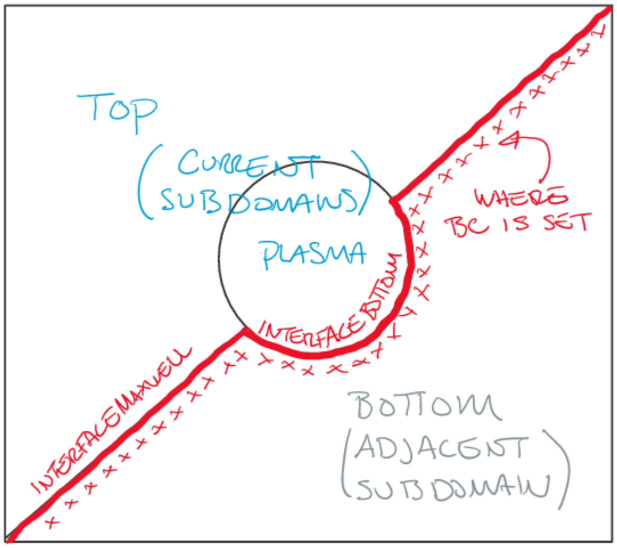

Figure A.2: Unit cell domain showing subdomain division. "Top" and "Plasma" contain one set of field variables, and "Bottom" has another set. Virtual boundary conditions are then required to pass the solution across the interior (red) and exterior boundary conditions

A.1.3 Solvers

Two sets of flux and source equations are set up for the real and imaginary domains.

A.1.4 Boundary conditions

A Bloch periodic virtual boundary condition is assigned at the domain boundaries (which are now also subdomain boundaries). The Bloch BC app takes in the real and imaginary fields, performs the phase shift, and assigns the result to the ghost cells of the fields at the opposite boundary. The app function have been reproduced below.

Another virtual boundary condition is needed on the interior subdomain boundary between the upper and lower field variables (see boundary in red in Figure A.2).

```
  void bloch_periodic_bc::bc_q(
    const real* q_in, const solverVariables_t* pFV, real* q_out) const
{
    // q_in = [realE_x, realE_y, realE_z, realB_x, realB_y, realB_z,
    //         imagE_x, imagE_y, imagE_z, imagB_x, imagB_y, imagB_z]
    // q_out = [realE_x, realE_y, realE_z, realB_x, realB_y, realB_z,
    //         imagE_x, imagE_y, imagE_z, imagB_x, imagB_y, imagB_z]

    // Real and imaginary fields are combined in a complex field
    q_comp[0] = std::complex<double> (q_in[0],q_in[6]);
    ...

    // Bloch periodic boundary condition is performed
    for (int var=0;var<6;var++) {
        for (int i=0;i<3;i++) {
            if (pFV->R[0][i] > 0.) {
                q_comp[var] = q_comp[var]*std::exp(j*_k[i]*_a[i]);
            }
            if (pFV->R[0][i] < 0.) {
                q_comp[var] = q_comp[var]*std::exp(-j*_k[i]*_a[i]);
            }
        }
    }

    // Complex fields are separated into their real and complex parts
    // and assigned to q_out
    q_out[0]  = std::real(q_comp[0]);
    ...
}
```

A.1.5 Initial condition

To indiscriminately excite as wide a range of frequencies and directions of waves as possible, a circular sinc function is initialized in the field, away from any points of symmetry (Figure A.3).

A.2 Example

In the example `user_runs\whitney_thomas\ppc\5_moment\bloch_periodic.py` a series of simulations is run with different wave vectors k. Fourier transforms are performed on probe field data to extract dominant frequencies for each simulations. These frequencies are then plotted versus wave number to create a dispersion relation, or band diagram, for the crystal (see Figure A.3).

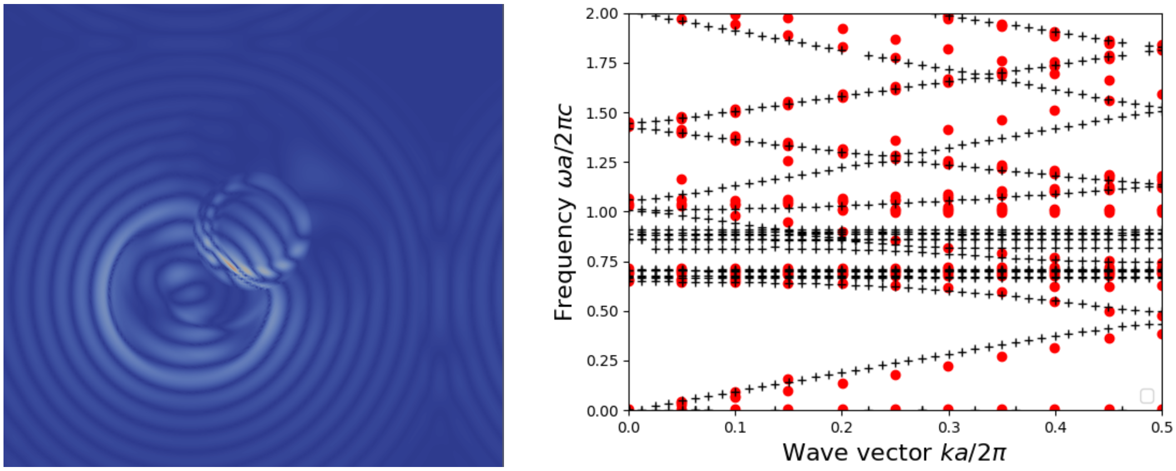

Figure A.3: (Right) initial condition with circular sinc pulse, and (left) a band diagram generated using the WARPXM implemented Bloch boundary conditions (red dots) compared to bands generated by another program, Meep (+).

Appendix 2

LACUNA BASED OPEN BOUNDARY CONDITION IMPLEMENTATION IN WARPXM

B.1 Motivation for open boundary conditions

There are many situations in plasma physics (and in fluid dynamics in general) where the region of interest is small compared to the distances information can propagate over the simulation time. Say, when a plasma is being irradiated by microwaves that aren't entirely absorbed, or plasma waves produced near a wall from sheath formation propagate into the bulk plasma, or a hurricane moving in a jet stream. If an artificial wall is simulated at the edges of the regions of interest, wave energy will be reflected back into the domain, skewing results. If the domain was made large enough that information could not reach the boundaries during the simulation, then large amounts of computation time would have to be spent advancing an effectively useless solution.

To solve this problem, boundary conditions that allow information to pass freely out of a simulation region are necessary. These "open" boundary conditions use various techniques to do this effectively. An excellent summary of the history of open boundary condition methods can be found in [16] by E.T. Meier, et al. While a number of simple open boundary conditions are adequate over short periods or with linear hyperbolic equations (zero normal derivative (ZND), or perfectly matched layers (PML)) they will accumulate error over long simulations, or mixed parabolic-hyperbolic systems.

A lacuna-based open boundary condition (LOBC) is proposed by E.T. Meier, et al, in [16]. The LOBC works by passing the interior solution to an exterior auxiliary variable via a source term. The auxiliary solution is then effectively damped out before reaching the exterior boundary, ensuring that information about the boundary cannot re-enter the interior domain.

B.2 Lacuna-based open boundary condition theory

The lacuna-based boundary condition (LOBC) is based on the fact that after a wave has passed, a fluid will return to its previous state. This quiescent region immediately following a wave is called a lacuna. The LOBC takes advantage of this idea by assuming that the lacuna of a wave is in the same state than if that wave had never passed by. In this case, if an earlier wave were suddenly "deleted" from the history of an auxiliary variable, the later solution will not be effected, leaving the boundary of the interior domain unchanged.

To see this in practice, we take an arbitrary PDE, written in flux-source form,

$$\frac{\partial \mathbf{q}}{\partial t} + \nabla \cdot \mathbb{F}(\mathbf{q}) = \mathbf{S}(\mathbf{q}), \tag{B.1}$$

where q is the interior variable, $\mathbb{F}$ is the flux, and $\mathbf{S}$ is the source. An exterior variable w is advanced with a similar system, except that it includes an extra source term $\mathbf{\Omega}(\mathbf{q})$,

$$\frac{\partial \mathbf{w}}{\partial t} + \nabla \cdot \mathbb{F}(\mathbf{w}) = S(\mathbf{w}) + \Omega(\mathbf{q}). \tag{B.2}$$

The variables w and q are related through a transition variable μ, which varies smoothly from 0 in the interior to 1 in the exterior region (see Figure B.3). The source term functions to transfer the interior solution to the auxiliary solution so that $w = q$ at the open boundary (the boundary between the transition and exterior regions). The value of w just outside this boundary is used as the boundary condition on q.

This set up alone will not prevent information from reflecting off of the exterior boundary and re-entering the interior domain through the boundary condition on q. To prevent this, the solution on w is periodically reintegrated with source $\Omega(q) = 0$ for some period of time. This effectively erases the leading edge of the wave front. When the reintegration and quiescent times are chosen appropriately, the wave front will always be erased before reaching the exterior boundary.

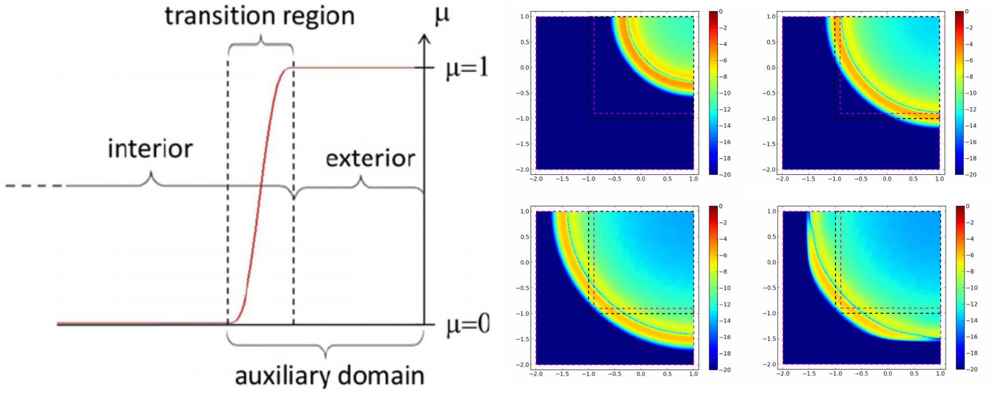

Figure B.1: LOBC domain schematic [16] (left), and a 2D EM wave pulse propagating into an LOBC exterior domain and subsequent reintegration [31](right).

B.3 Implementation of the LOBC in WARPXM

WARPXM is well suited for efficient implementation of the LOBC. The code is modular: new boundary conditions, source terms, and equation sets can easily be added without touching much of the code. Variables and equation sets can be assigned to single or multiple subdomains, allowing auxiliary variables to only exist and be evolved in auxiliary domains.

Differing slightly from the method described in [16], the auxiliary solution was not reintegrated periodically. Instead, a second auxiliary variable w_{lacuna} was evolved simultaneously with the source term set to zero for some amount of time following a “reintegration.” At what would have been a reintegration time, the w_{lacuna} is swapped with w, and then zeroed. The cycle is repeated over the duration of the simulation.

Evolving a second auxiliary variable prevents having to store source values and perform the periodic reintegration, which would require significant modifications to the WARPXM framework. This also spreads out the load of the reintegration over all time steps. Swapping pointers for w and w_{lacuna}, instead of copying further reduces memory usage and time.

The structure of the problem setup is as follows:

- A mesh is created the has, at a minimum, an interior and exterior subdomain with a transition subdomain separating the two.

- Interior variables and equation sets are initialized as usual on the interior and transition subdomains.
- Auxiliary variables w and w_{lacuna} and their equation sets are initiated on the transition and exterior subdomains.
- On the transition subdomain alone, the transition variable is initialized and its gradient calculated.
- The gradient, along with the flux application for the interior variable q is passed to auxiliary variable source term Ω for w and w_{lacuna}. The source term for w_{lacuna} also includes a reintegration and lacuna time period to determine when to set the source to zero.
- A boundary condition on the transition-exterior boundary assigns values of w to the ghost values of q.
- As the simulation advances a reintegration time period, set by the user, triggers w and w_{lacuna} to be swapped, and then zeros w_{lacuna} .

To implement the LOBC in WARPXM, the following new capabilities were added:

- LOBC source term for $\Omega(q)$.
- A timed variable swap host action, which takes the place of the auxiliary variable reintegration.
- Generic virtual boundary condition that copies one variable to the ghost cell of another. This is used for the open boundary condition on q.
- Helper functions to simplify simulation setups that use LOBCs.

B.3.1 The LOBC source application

To find an appropriate expression for the source term $\Omega(q)$, we can replace all the ws in Eq. B.2 with the equivalent μq,

$$\frac{\partial \mu \mathbf{q}}{\partial t} + \nabla \cdot \mathbb{F}(\mu \mathbf{q}) = S(\mu \mathbf{q}) + \Omega(\mathbf{q}). \tag{B.3}$$

μ is not a function of time, and assuming that $\mathbb{F}$ and S are linear functions of q, then we can extract μ to get,

$$\mu \frac{\partial \mathbf{q}}{\partial t} + \nabla \cdot \mu \mathbb{F}(\mathbf{q}) = \mu S(\mathbf{q}) + \Omega(\mathbf{q}). \tag{B.4}$$

Performing a vector-scalar product rule, and collecting terms we get

$$\Omega(\mathbf{q}) = \mu \left(\frac{\partial \mathbf{q}}{\partial t} + \nabla \cdot \mathbb{F}(\mathbf{q}) - S(\mathbf{q}) \right) + \mathbb{F}(\mathbf{q}) \cdot \nabla \mu. \tag{B.5}$$

The expression in parentheses is the evolution equation for q, and is equal to zero. What remains is a simple equation for $\Omega(q)$ that depends only on the flux $F(q)$ and the gradient of the transition variable:

$$\Omega(\mathbf{q}) = \mathbb{F}(\mathbf{q}) \cdot \nabla \mu. \tag{B.6}$$

In the implementation for WARPXM, an application is created that takes as inputs the flux application for q, as well as the gradient of μ ($[\partial\mu/\partial x, \partial\mu/\partial y, \partial\mu/\partial z]$) calculated previously. The application is also made time dependent, so that it may be turned off during the quiescent period in the reintegration variable such that,

$$\Omega(\mathbf{q}, t) = \ell(t) F(\mathbf{q}) \cdot \nabla \mu, \tag{B.7}$$

where $\ell(t) = 0$ for $nt_{reint} < t < nt_{reint} + t_{lacuna}$, $n = 1, 2, 3, ..$, and one at all other times.

The flux $F(q)$ is the same analytic flux as calculated in the evolution equations for q. To make the source app general use (regardless of problem being solved), the app is passed a flux app in the input file.

```
<w_lobc_source>
  Type = application
```

```
  Kind = LOBC_SOURCE
  ReintegrationTime = 2.0
  LacunaTime = 0.0
  ExteriorVariable = [6, 7, 8, 9, 10, 11]
  GradientMu = [18, 19, 20]
  InteriorVariable = [0, 1, 2, 3, 4, 5]
  <q_flux_app>
    Type = application
    Kind = maxwell
    skin_depth_norm = 1.0
    omega_p_norm = 1.0
    Field = [0, 1, 2, 3, 4, 5]
  </q_flux_app>
</w_lobc_source>
```

When the `setup()` of the LOBC source (`wmapplication_lobc_source.cc`) is called during simulation initialization, the crypt set is searched for an application

```
std::vector<std::string> names = wxc.getNamesOfType("application");
```

If one is found the cryptset for the flux application block is extracted, and used to create the `WmApplication` object `_flux_app`.

```
if (names.size()==1)
{
  const WxCryptSet& subwxc = wxc.getSet(names[0]);
  _flux_app.reset(WxCreatorMap<WmApplication>::getNew(subwxc.get<std::string>("Kind")));
  _flux_app->setup(subwxc);
}
```

and finally the setup function for that application is called.

During the simulation the `internal_flux()` function of the `_flux_app` is called and used to calculate the source term at that node

```
// Calculate the internal flux
std::vector<std::vector<real>> internalFlux(pEG->num_dims, std::vector<real> (num_components, 0.));
_flux_app->internal_flux(q, aux, pEG, internalFlux);
```

```
if (std::fmod(t, _reint_time) >= _lacuna_time)
{
  for (size_t i=0; i < num_components;++i)
  {
    for (size_t j = 0; j < pEG->num_dims; ++j)
    {
      source[i] += aux[j] * internalFlux[j][i];
    }
  }
}
```

B.3.2 Reintegration: the fill_value and timed_swap host actions

Performed with the `fill_value` and `timed\_swap` host actions.

B.3.3 Boundary condition at the open boundary

WARPXM treats normal boundary conditions by assigning values to the nodes on ghost elements (additional elements that WARPXM appends to the element list from the imported mesh). VBCs differ from normal boundary conditions in WARPXM in that there are no ghost elements created on these interior subdomain boundaries.

B.4 Using LOBCs in WARPXM

B.4.1 Mesh

To run a simulation with an LOBC a mesh file must be created with at least three subdomains:

- “interior” - The interior subdomain can either be all of the normal simulation domain (excepting the transition region) or just the region in the domain adjacent to the transition region.
- “transition” - The transition subdomain is part of the normal simulation domain and completely separates the interior from the exterior subdomains. The transition region

Figure B.2: Examples of meshes that are LOBC ready.

should be at minimum 10 elements across.

- “exterior” - This is the only region that is outside the normal simulation domain. The only subdomain it shares a boundary with is the transition subdomain. The larger the exterior domain, the larger the added computational cost, but the less frequent reintegrations need to occur. As reintegrations add very little to computation time in this implementation, it is better to have a smaller exterior subdomain. 3 to 4 times the width of the transition region is sufficient.

And two node sets:

- “transBoundary” - Separates the interior and transition subdomains.
- “openBoundary” - Separates the transition and exterior subdomains. Also constitutes the normal simulation domain boundary.

B.4.2 Variables

Variables to be initialized:

- **Interior variables:** These are the simulation variables, and are initialized everywhere in the normal simulation domain
  - Subdomains: “interior”, “transition”
  - Virtual subdomains: “exterior”
  - Initial condition: what ever is necessary for the problem
- **Exterior variables w and w_{lacuna}:** This are the auxiliary variables that the interior solution is passed to through the source term in the transition region.
  - Subdomains: “transition”, “exterior”
  - Virtual subdomains: None
  - Initial condition: must be consistent with the interior variable such that $w = \mu q$, where q is the interior variable.

- **Transition variables μ and $\nabla\mu$:** The transition variables only exist in the transition region
  - Subdomains: “transition”
  - Virtual subdomains: None
  - Explodable: False (This prevents WARPXM from creating copies of the variable for Runge-Kutta intermediate values.)
  - Initial condition: μ must be a C^1 continuous function with the boundary conditions $\mu|_{int} = 0$, $\mu|_{ext} = 1$, and $\nabla\mu \cdot \hat{n}|_{int,ext} = 0$, where $\hat{n}$ is the normal at the interior or exterior boundary.
  - Caution!: When $\nabla\mu$ is calculated from a specified μ with a gradient variable adjuster, boundary values of μ must be specified. Setting zero Neumann (zero first derivative) boundary conditions on all physical boundaries is sufficient.

    As only $\nabla\mu$ is required, and if it is known can specified without having to initialize μ and calculate its gradient.

B.4.3 Assigning flux and source applications

Physics apps for fluxes and sources are assigned to the interior and exterior variables alike.

In addition to the physics apps, an LOBC source ($\Omega(q)$) is applied only to the exterior variables, and only in the transition subdomain.

B.4.4 Setting virtual and traditional boundary conditions

- Non-LOBC boundaries are set as usual.
- Physical boundary conditions on the exterior subdomain should not cause backward propagation of information through the open boundary in the time between reintegration. Zero Neumann or a continuation of the physical boundary conditions from the interior domain are good options.
- Boundary condition on μ should be zero Neumann (zero gradient) on all transition subdomain boundaries.

- Boundary condition on "transitionBoundary" for auxiliary variables should be a zero Dirichlet.
- Boundary condition on "openBoundary" for interior variables will use the virtual boundary condition.

B.4.5 Choosing reintegration and quiescent time periods

Reintegration and quiescent time periods should be chosen so that the fastest wave speed in the system will not travel the width of the exterior region (or twice that width if reflection is allowed) during a reintegration period.

If a is the fastest wave speed, L_e and L_t are the exterior and transition domain widths, some advisable bounds on times are

$$t_{integration} \leq L_e/a + t_{quiescent} \quad : \quad t_{quiescent} \approx L_t/a. \tag{B.8}$$

B.5 Example: 2D Maxwell equations

The example in Figure B.3 was run using the `2D_maxwell_lobc.py` input file. The boundary conditions in y are conducting wall. A wave train emanates from the right boundary and passes through transition region to the auxiliary variable. In the last frame, the auxiliary solution has been reintegrated and wave front has receded from the left wall. The domain is 0.5×7 nu, the normalized speed of light is 1, and the quiescent and reintegration times are 4 and 6, respectively

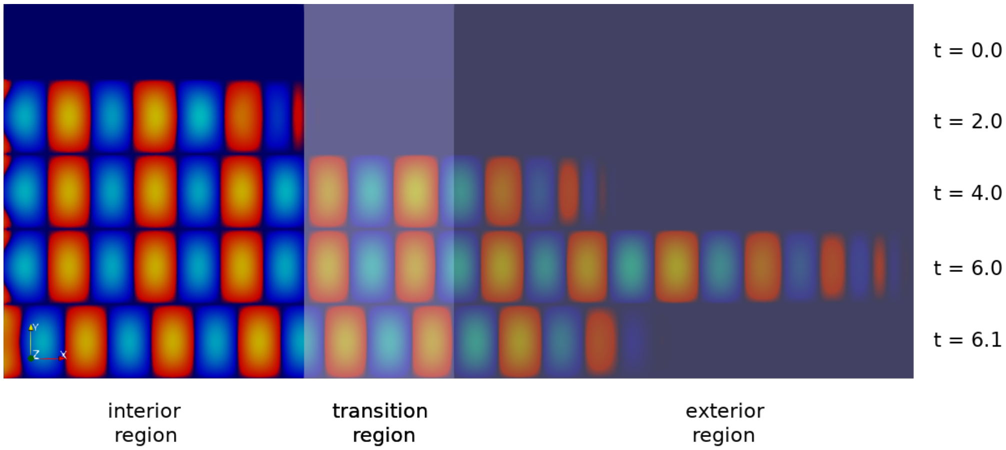

Figure B.3: A 2D EM wave propagating into an LOBC exterior domain and subsequent reintegration.

BIBLIOGRAPHY

[1] Malgorzata Celuch-Marcysiak and Wojciech K. Gwarek. Spatially Looped Algorithms for Time-Domain Analysis of Periodic Structures. *IEEE Transactions on Microwave Theory and Techniques*, 43(4):860–865, 1995.

[2] Henry N. Chapman, Petra Fromme, Anton Barty, and Thomas A. White. Femtosecond X-ray protein nanocrystallography. *Nature*, 470(7332):73–78, 2011.

[3] Guanying Chen, Jangwon Seo, Chunhui Yang, and Paras N. Prasad. Nanochemistry and nanomaterials for photovoltaics. *Chemical Society Reviews*, 42(21):8304, 2013.

[4] Shanhui Fan, Wonjoo Suh, and J. D. Joannopoulos. Temporal coupled-mode theory for the Fano resonance in optical resonators. *J. Opt. Soc. Am. A*, 20(3):569–572, 2003.

[5] Weili Fan, Xinchun Zhang, and Lifang Dong. Two-dimensional plasma photonic crystals in dielectric barrier discharge. *Physics of Plasmas*, 17(11), 2010.

[6] Hai feng Zhang, Li Ma, and Shao bin Liu. Study of periodic band gap structure of the magnetized plasma photonic crystals. *Optoelectronics Letters*, 5(2):112–116, 2009.

[7] Xiaohua Huang and Mostafa A. El-Sayed. Gold nanoparticles: Optical properties and implementations in cancer diagnosis and photothermal therapy. *Journal of Advanced Research*, 1(1):13–28, 2010.

[8] Jd John D Joannopoulos, Steven Johnson, Joshua N Jn Winn, and Rd Robert D Meade. *Photonic crystals: molding the flow of light.* 2008.

[9] Sajeev John. Strong localization of photons in certain disordered dielectric superlattices. *Physical Review Letters*, 58(23):2486–2489, 1987.

[10] J. C. Knight, T. A. Birks, P. St. J. Russell, and J. P. de Sandro. Properties of photonic crystal fiber and the effective index model. *Journal of the Optical Society of America A*, 15(3):748, 1998.

[11] Tomas Kohoutek, Mikhail Parchine, Maria Bardosova, Hiroshi Fudouzi, and Martyn Pemble. Large-area flexible colloidal photonic crystal film stickers for light trapping applications. *Optical Materials Express*, 8(4):960, 2018.

[12] Jan Krajczewski, Karol Kołątaj, and Andrzej Kudelski. Plasmonic nanoparticles in chemical analysis. *RSC Adv.*, 7(28):17559–17576, 2017.

[13] T.F. Krauss. Pbf-pic. https://www.st-andrews.ac.uk, 2011. Accessed: 2018-08-08.

[14] J. Lo, J. Sokoloff, T. H. Callegari, and J. P. Boeuf. Reconfigurable electromagnetic band gap device using plasma as a localized tunable defect. *Applied Physics Letters*, 96(25), 2010.

[15] Boris Luk'Yanchuk, Nikolay I. Zheludev, Stefan A. Maier, Naomi J. Halas, Peter Nordlander, Harald Giessen, and Chong Tow Chong. The Fano resonance in plasmonic nanostructures and metamaterials. *Nature Materials*, 9(9):707–715, 2010.

[16] E. T. Meier, A. H. Glasser, V. S. Lukin, and U. Shumlak. Modeling open boundaries in dissipative MHD simulation. *Journal of Computational Physics*, 231(7):2963–2976, 2012.

[17] meyavuz. Periodic band gap (pgb) waveguide and propagation - fdtd simulation (photonic crystal). https://www.youtube.com/watch?v=gZkFVco4kL4, 2011. Accessed: 2018-08-08.

[18] S T Miller and U Shumlak. A multi-species 13-moment model for moderately collisional plasmas. 082303(2016), 2017.

[19] Sean Miller. Modeling collisional processes in plasmas using discontinuous numerical methods. 2016.

[20] C. D. Munz, P. Omnes, R. Schneider, E. Sonnendrücker, and U. Voß. Divergence Correction Techniques for Maxwell Solvers Based on a Hyperbolic Model. *Journal of Computational Physics*, 161(2):484–511, 2000.

[21] Ardavan F. Oskooi, David Roundy, Mihai Ibanescu, Peter Bermel, J. D. Joannopoulos, and Steven G. Johnson. Meep: A flexible free-software package for electromagnetic simulations by the FDTD method. *Computer Physics Communications*, 181(3):687–702, 2010.

[22] S.G. Parsons and J. Hopwood. Millimeter Wave Plasma Formation Within a 2D Photonic Crystal. *IEEE Electron Device Letters*, 38(11), 2017.

[23] Li-Mei Qi and Ziqiang Yang. Modified Plane Wave Method Analysis of Dielectric Plasma Photonic Crystal. *Progress In Electromagnetics Research*, 91:319–332, 2009.

[24] Limei Qi, Chao Li, Guangyou Fang, and Xiang Gao. The Absorbing Properties of Two-Dimensional Plasma Photonic Crystals. *Plasma Science and Technology*, 17(1):4–9, jan 2015.

[25] R. Rumpf. Presentation: 21st Century Electromagnetics - Lecture 14. University of Texas at El Paso., 2014.

[26] O Sakai, T Sakaguchi, Y Ito, and K Tachibana. Interaction and control of millimetre-waves with microplasma arrays. *Plasma Physics and Controlled Fusion*, 47(12B):B617–B627, dec 2005.

[27] Osamu Sakai, Takui Sakaguchi, and Kunihide Tachibana. Photonic bands in two-dimensional microplasma arrays. I. Theoretical derivation of band structures of electromagnetic waves. *Journal of Applied Physics*, 101(073304), 2007.

[28] Osamu Sakai, Kunihide Tachibana, and Rotman W. Plasmas as metamaterials: a review. *Plasma Sources Science and Technology*, 21(1):013001, feb 2012.

[29] K. Sakoda. *Optical properties of photonic crystals*. Springer, 2001.

[30] U. Shumlak, R. Lilly, N. Reddell, E. Sousa, and B. Srinivasan. Advanced physics calculations using a multi-fluid plasma model. *Computer Physics Communications*, 182(9):1767–1770, 2011.

[31] Eder M. Sousa. A Blended Finite Element Method for Multi-fluid Plasma Modeling. 2014.

[32] Allen Taflove. *Computational electrodynamics : the finite-difference time-domain method*. Artech House antennas and propagation library. Artech House, Boston, 3rd ed. edition, 2005.

[33] Jérémie Teyssier, Suzanne V. Saenko, Dirk Van Der Marel, and Michel C. Milinkovitch. Photonic crystals cause active colour change in chameleons. *Nature Communications*, 6:1–7, 2015.

[34] J. Topolancik, B. Ilic, and F. Vollmer. Experimental observation of strong photon localization in disordered photonic crystal waveguides. *Physical Review Letters*, 99(25):2–5, 2007.

[35] B Vasic and R Gajic. Tunable gradient refractive index optics using graded plasmonic crystals with semiconductor rods. *Journal Of the Optical Society Of America B-Optical Physics*, 29(1):79–87, 2012.

[36] B Wang and M A Cappelli. A tunable microwave plasma photonic crystal filter. *Applied Physics Letters*, 107, 2015.

[37] B Wang and M A Cappelli. A plasma photonic crystal bandgap device. *Applied Physics Letters*, 108, 2016.

[38] B Wang and M A Cappelli. Waveguiding and bending modes in a plasma photonic crystal bandgap device The Simulation of the Modes in a Photonic Crystal Bend Waveguide for Two Different Compositions AIP Conf Waveguiding and bending modes in a plasma photonic crystal bandgap device. *Appl. Phys. Lett. Proc.*, 6(10):65015–161101, 2016.

[39] B. Wang, R. Lee, R. Colon, and M. A. Cappelli. A microstrip photonic crystal bandgap device with a switchable negative epsilon plasma element. *Microwave and Optical Technology Letters*, 59(12):3097–3101, 2017.

[40] Yongjie Wang, Lifang Dong, Weibo Liu, Yafeng He, and Yonghui Li. Generation of tunable plasma photonic crystals in meshed dielectric barrier discharge. *Physics of Plasmas*, 21(7):1–6, 2014.

[41] E. Yablonovitch, T. J. Gmitter, and K. M. Leung. Photonic band structure: The face-centered-cubic case employing nonspherical atoms. *Physical Review Letters*, 67(17):2295–2298, 1991.

[42] Eli Yablonovitch. Inhibited spontaneous emission in solid-state physics and electronics. *Physical Review Letters*, 58(20):2059–2062, 1987.